P1R.4 HIGH RESOLUTION AIRBORNE RADAR DUAL-DOPPLER TECHNIQUE

Rick Damiani*, Samuel Haimov, and Gabor Vali
Department of Atmospheric Science, University of Wyoming

1. INTRODUCTION

Multidimensional analyses of cloud inhomogeneities or of atmospheric turbulence characteristics long represented an almost unaffordable task. Aircraft penetrations, with in situ instrumentation alone, lack to offer a comprehensive set of observations, being limited to one dimensional samplings and temporally constrained by the small time scales of the cloud. Ground-based remote sensing can partially fill in a broader picture. X- or S-band radar ground installations have been used since the 1960s to study the dynamical structure of clouds, including convective ones. The potential of W-band millimeter wavelength radars has also been demonstrated (Lhermitte 1987, 1988; Kollias et al. 2001). The high sensitivity of 95 GHz radars with respect to cloud droplets and their high spatial resolution allow for a more thorough view of the cloud environment in terms of both small scale structural features and mean dynamic properties. Multiple-Doppler radar techniques have also been proposed to study the kinematics of atmospheric phenomena, from stratiform clouds (Heymsfield 1979), to convective clouds (Lhermitte 1975; Ray et al. 1975; Kropfli and Miller 1976; Ray et al. 1980; Knupp and Cotton 1982; Sun and Crook 1998; Gao et al. 2004), to clear-air boundary layers (Kropfli and Hildebrand 1980; Atkins et al. 1995). Ground-based remote sensing, though capable of providing high temporal resolution samples of the target volume, suffers from several limiting factors. Foremost, scientific observations are restricted to phenomena occurring in the area covered by the radars. Secondly, their scanning outcome is usually lessened in the vertical direction. Thirdly, the interpretation of in situ data in the context of the radar retrieved cloud structure is hampered by the general temporal and spatial offsets.

The design and development of an airborne meteorological radar was first advocated by Lhermitte (1971). When coupled with an airborne platform, the merging of in situ observations with radar data yields a multifaceted insight of the cloud physics. On one hand, mobile platforms offer the ability to gather data in multiple regions of meteorological interest, rather than in one location dictated by a fixed radar. On the other hand, the radar retrieved reflectivity and velocity fields complete a picture that would, otherwise, only rely on the cloud thermodynamic characteristics at flight level.

First tests on the feasibility of airborne pseudo-dual-Doppler analyses performed via a vertically scanning single-beam radar, and comparisons with a ground-based dual-Doppler network are given by Jorgensen et al. (1983); Ray et al. (1985); Hildebrand and Mueller (1985). For these configurations, the lengthy time needed to collect data by orienting a single antenna beam along multiple directions impairs the resolution and the retrieved velocity accuracy. Dual-scanning beam airborne radars have been proposed (Jorgensen et al. 1983, 1996; Hildebrand et al. 1996), where the reduced time lag between illuminations of same spatial volumes is on the order of a minute or more and the spatial resolution in the hundreds of meters. An alternative solution is an aircraft-based fixed dual-beam (dual-antenna) Doppler radar. A first description of such a configuration for an X-band radar, with a discussion of the potential analysis errors, is given in Heymsfield et al. (1996). A similar set-up is presented in Damiani et al. (2004) for a W-band device. For such type of configurations the aircraft provides the necessary motion to scan the same sample volume along two fixed beam directions, with a short time lag between the two illuminations. A typical time interval of 10 s (at ranges $\leq$3 km) reduces the target evolution and advection effects. From the analysis of two independent radial velocity components, an estimate of the target velocity in the plane determined by the beams can be inferred. This leads to the retrieval of a 2-D kinematic field.

Besides the advantages in terms of data collection time, the airborne fixed multi-beam radar installation offers a simplified and cost-effective design with respect to a single or dual scanning-beam one. It further yields an along-flight-track resolution of 30-40 m which is at least an order of magnitude higher than that of the currently used scanning configurations, and it is prone to less uncertainty in the beam pointing angles and thus on the final retrieved velocity. Furthermore, if the beams scan a vertical plane, an immediate retrieval of vertical air motion can be achieved by removing the aircraft (AC) motion and particle fall-speed, without the necessity of integrating the continuity equation. The two-antenna set-up can further be used to estimate reflectivity attenuation via the 'stereoradar' or 'dual-beam' approach and to retrieve cloud microphysical characteristics of clouds (Guyot and Testud 1999; Lopez et al. 2000).

In this paper, we offer a technique to merge and analyze airborne fixed-dual-beam Doppler radar data in either vertical or horizontal planes of scans. The technique has been recently applied to the Wyoming Cloud Radar (WCR) installation aboard the University of Wyoming KingAir (UWKA), with first scientific results documented in Geerts et al. (2004) for the investigation of a clear-air boundary layer density current, and in Damiani et al. (2004, 2005) for cumulus cloud studies.

The WCR is a 3.2 mm wavelength (95 GHz) Doppler radar (Pazmany et al. 1994). Details of its multi-beam UWKA installation are given in Section 2. Sections 3 - 4.1 illustrate how the data from the two beams are re-gridded onto a Cartesian mesh advecting with the mean wind speed, and how the grid parameters can be customized to accurately follow the AC trajectory. The grid resolution

* *Corresponding author address:* Rick Damiani, Dept. of Atmos. Sci., University of Wyoming, 1000 E. University Ave., Laramie WY, 82071; E-mail: rickdami@uwyo.edu

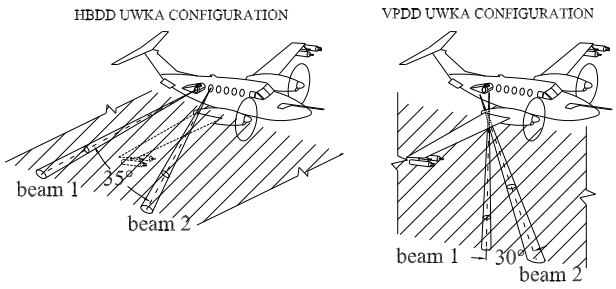

FIG. 1. WCR dual-Doppler antenna beam configurations aboard the UWKA.

can be adjusted to account for the range-degrading radar beam resolution or to enhance the details in specific areas of the scanned region.

Sections 4.2 - 4.4 describe the velocity inverse decomposition problem to be solved for every grid cell; it consists of a system of equations carrying the information on the measured radial velocities, solved via a weighted least-squares method. In order to avoid contamination of the velocities by out-of-plane wind components, an estimate of the ambient wind needs to be introduced in the calculation algorithm. The data weighting functions are based on the relative geometry of the data points and the grid cell centroids, on the entity of the beam out-of-plane components, and on the data signal-to-noise ratio (SNR).

The technique error sources are discussed in Section 5; they include random errors due to the spread of the Doppler spectrum, systematic errors due to uncertainties in the beam pointing directions, AC motion, ambient mean wind, and interpolation approach.

In Section 6, two case studies related to horizontal and vertical cumulus cloud scans are presented together with an upper bound estimate of their dual-Doppler analysis errors. Conclusions are summarized in Section 7. A description of an IDL® based software package implementing the technique is available at `http://www-das.uwyo.edu/wcr/idl/wcrdddoc.pdf`.

2. AIRBORNE MULTI-BEAM RADAR AND DUAL-DOPPLER CONCEPT

Table 1 reports the principal specifications of the WCR. Fig. 1 shows a schematic of the dual-beam antenna configurations available on board the UWKA. Four antennas are mounted on the aircraft: two look down along the vertical plane normal to that of the wings; the other two scan a starboard horizontal plane. The first pair (nadir and nadir-forward antennas) allows for the retrieval of the scatterer velocity in the vertical plane aligned with the aircraft track (*VPDD*, Vertical Plane Dual-Doppler); the second (side and side-forward antennas) can be used to retrieve the horizontal 2-D velocity field (*HBDD*, Horizontal Beam Dual-Doppler).

In Fig. 2, the basic concept of the airborne dual-Doppler is illustrated. The return signals associated with two fixed radar beams (antennas) are combined to provide two independent measurements of the scatterer

WCR Operational Parameters	Value(s) and/or Range
Frequency	94.92 GHz (λ =3.16 mm)
Nominal Peak Power	1.6 kW (1% duty cycle)
Nominal Pulse Length	100, 250, 500 ns
Pulse Repetit. Frequency (PRF)	1-20 kHz
Receivers	2
- dynamic range	$>$70 dB
- bandwidth	10, 5, 2 MHz
Antennas	4; 5 fixed beam positions
- aperture	0.30, 0.30, 0.38, 0.46 m
- beamwidth	0.8, 0.8, 0.6, 0.5°
- gain	45, 46, 48, 50 dB
- polarization (linear)	one *dual* (H,V), three *single*
Doppler Velocity	
- pulse-pair processor	$\pm$15.8 m s^{-1} @ 20 kHz PRF
- FFT spectrum	32 or 64 spectral lines
Volume Resolution	
- 250 ns, 0.3 m antenna	37 x 12 x 15 m @ 1 km 37 x 36 x 39 m @ 3 km
Minimum Detectable Signal (250 ns, 500 averaged pulses, 0.3 m antenna, @1 km)	-30 dBZ (1 std. dev. above mean noise)

Table 1. Wyoming Cloud Radar Parameters.

mean velocity in a given illuminated volume. Due to the stochastic nature of the target and the sources of the measurement errors, more than just two radar illuminations will be used, making the problem overdetermined, even though the directions of scan will remain nearly dependent on the main two. Each data point is characterized by the pair ($prof$,r), where $prof$ is the indexed radar return from M radar pulses, and r is the *rangegate* number related to the sampled distance along the range. A typical WCR profile dwell time is 25 to 30 ms and the number of rangegates is between 50 and 150, with sampling interval from 15 to 45 m.

The mathematical problem consists of retrieving the velocity vector that decomposes along the measured radial components (cf. Section 4.4). The sought velocity is a 3-D vector, but only two independent components are effectively measured. Thence, one may hope to resolve with sufficient accuracy just the projection of the velocity on the plane determined by the beam directions. However, an estimate of the so-called 'cross-plane' component is necessary. The attitude of the aircraft can, in fact, yield an erroneous reading of the in-plane velocity due to the contamination of the radial velocities by the across-plane wind when the beams are forced out-of-plane. For this purpose an assumed horizontal wind vector (usually based on in situ measurements in the vicinity of the observed clouds) is also employed.

This methodology is feasible as long as the volume scanned by one of the beams is observed by the other after a time interval shorter than the characteristic evolu-

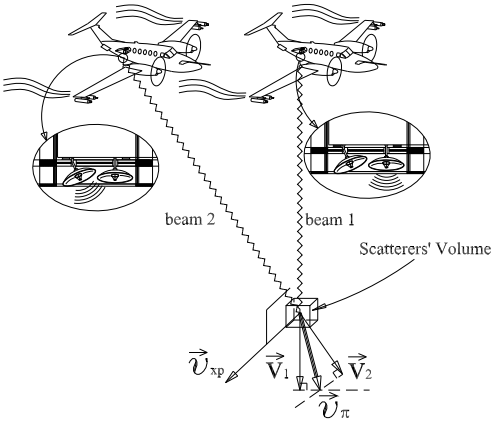

FIG. 2. Dual-Doppler main concept: a given scatterer volume is illuminated by the two beams at short distance in time. $\vec{V}_1$ and $\vec{V}_2$ are the Doppler mean radial velocities; $\vec{v}_{xp}$ denotes the 'cross-plane' component, i.e.: the non-measured component of the velocity, normal to the plane of the beams. $\vec{v}_\pi$ is the retrieved scatterer velocity in the plane of the beams.

tion time-scale of the scatterer volume. At typical aircraft (AC) airspeeds greater than 90 m s^{-1} and at typical WCR maximum ranges ($\sim$3 km) the time-lag is on the order of 15 s; at minimum ranges it is on the order of 1 s.

The choice of the beam geometry is dictated by the requirement of obtaining accurate dual-Doppler retrievals and by the platform structural constraints. Under the boundaries imposed by the latter, the angle between the beam directions is calculated as a trade-off between two requisites. On one hand, the scanning directions should be kept as far apart as possible to maximize the vector independence. In the literature, e.g., Hildebrand et al. (1996), it is suggested that the directions from which two or more radial velocities are measured should differ by 30° or more; this number is also based on the classic dual-Doppler approach requiring the integration of the mass budget equation in a 3-D volume (Doviak and Zrnic 1993). On the other hand, the time lag between illuminations, proportional to the angle between the beams, should be kept small to reduce the target evolution effects. For the UWKA installation the antenna beams form angles near 30° (see Fig. 1). Moreover, one of the beams is mounted perpendicular to the AC normal direction of motion. This layout is recommended because it reduces the AC motion contribution into the radial velocity measurement (also decoupling the AC attitude deviations from straight and level flight), and it allows for a direct retrieval of vertical velocities (nadir antenna beam).

The steps necessary for the dual-Doppler analysis of a selected flight segment are:

1. Synchronize the data from the radar and AC data system.
2. Apply calibration and threshold to the reflectivity data (optional).
3. Correct radial Doppler velocities for Aircraft motion, via Inertial Navigation System (INS) and Global Positioning System (GPS) data.
4. Unfold aliased Doppler velocity.
5. Transform every data point from both beams to a common coordinate system.
6. Construct a Cartesian grid (mesh) onto which the data coming from the two beams will be interpolated. The grid advects with the estimated mean wind velocity.
7. Weight average the data from each beam in the vicinity of every grid point.
8. Solve the dual-Doppler *velocity inverse decomposition problem*.

In the following sections, some of these steps are explored in detail.

3. GRID CONSTRUCTION

The data coming from the two beams need be interpolated onto a common Cartesian grid, so to ensure the correct spatial mutual placement of the target features, and to allow for the solution of a velocity inverse decomposition problem for every grid cell. The grid can be thought to be translating with a mean wind or storm motion, so that the advection effects due to the time lag between illuminations are reduced (cf. Section 5.8).

The gridding and data point interpolation affect the quality of the retrieved velocities, hence special attention is dedicated to guarantee that the maximum number of points partake in the analysis. The flight pattern and the AC attitude influence the spatial orientation of the radar beams and the data point position. A constant heading flight, as for instance in straight-track boundary layer missions, would originate a different distribution of data points (radar scanned surface) when compared to a more complex flight trajectory where the three-dimensionality could be relevant.

On these premises, the dual-Doppler procedure was developed following two gridding layouts according to the type of flight pattern adopted. The first type, where the AC track can be approximated by a straight line, is hereafter referred to as *'straight-leg'*. The second type, referred to as *'curtain-leg'*, describes a more generic flight track and radar scanned surfaces (see Fig. 3).

In Fig. 4, the principal elements of the grid layout are illustrated. The grid will be constructed starting from the identification of its *corner points*. The resulting cell boundaries will be used to discern whether or not a data point belongs to the generic (i, j)-th cell. The technique also makes use of grid *center points* (referred to as *grid points*) for data weighting purposes and for the assignment of the final retrieved velocity. They are determined from the centroids of the cells. A curvilinear 2-D reference system $(O; \xi, \eta)$ tied to the principal directions of the grid is also shown in Fig. 4. Cell rows and columns are along the ξ and η direction, respectively. In case of

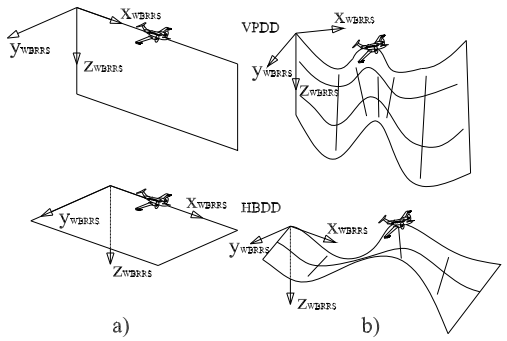

FIG. 3. The two different type of *flight-legs* considered in the dual-Doppler technique and the resulting scanned surfaces; a) *straight-leg*; b) *curtain-leg*. Indicated are also the WBRRS frames of reference.

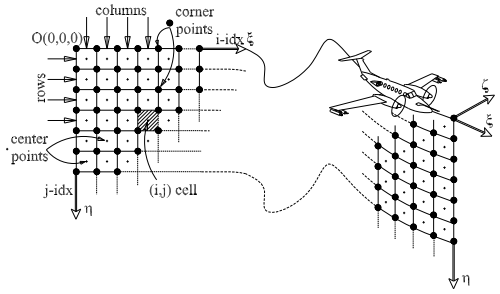

FIG. 4. Typical grid arrangement and definitions of *rows, columns, corner, center points, and the (ξ,η,ζ) reference system*. The illustration refers to VPDD.

a straight-leg grid the (ξ,η) directions are constant. For both straight and curtain-leg cases the third dimension of the grid, along ζ, is implicit and does not play a role until the beam points get assigned to the cells. Hereafter we will refer to this dimension as grid *swath*. A limit can be imposed on the maximum allowed swath to remove distant data points from the desired scanning plane.

Further reference systems adopted in the dual-Doppler technique will be described below. Their purpose is multifold: from the geometric characterization and interpolation of the beam data points, to the establishment of an air- (i.e., wind-) relative frame of reference; from the assessment of a local *'solution plane'* determined by the beam directions, to the correct introduction of the external wind information within each cell. In this paper, we will be generally using a VPDD configuration for illustration purposes without loss of generality; the extension to HBDD is straightforward.

UFRS. The first reference system is the ground (Earth's) reference system identified as *UFRS* (Unrotated Fixed Reference System) with x,y,z along East, North, vertical (Up). It may be thought as anchored to the Earth's surface directly below the initial position of interest of the AC center of mass (G).

ACRS. The Aircraft Reference System has origin in G, and the x-axis along the AC fuselage, the y-axis along the right wing and the z-axis pointing down. The AC attitude is referred to the ground reference system via the Eulerian angles ψ, θ, ϕ (i.e., AC heading, pitch and roll angles): they represent the transformation angles from UFRS to *ACRS*. Together with their time variation rates, they are used to determine the in-flight beam directions and to remove the aircraft motion from the measured radial Doppler velocities.

WBRRS. The Wind Based Rotated Reference System, *WBRRS* is the technique principal coordinate system, accounting for the mean advection of the target. In case of straight-leg, the WBRRS x-axis is aligned with the AC track mean course heading, z points down and y to the right of the track. For the curtain-leg cases, x is due East, z points down and y is determined according to the left hand rule. The origin moves with the assumed advection velocity. The latter can be an a-priori known constant, or the AC flight-level measured mean wind vector; it can also be locally adjusted for the measured wind at each data point, or set equal to the average velocity coming from the mean radar Doppler field. The latter estimate derives from averaging the recorded Doppler field and performing the velocity inverse decomposition retrieval on it (cf. Section 4.4).

The adopted advection velocity is subtracted from the AC ground speed (determined by INS and GPS) in order to achieve a good estimate of the AC air-relative velocity vector. The construction of the grid is based on the resulting AC track, i.e., relative to WBRRS. Scans of atmospheric features, within clouds for instance, will then be correctly placed in mutual relationship, both geometrically and physically. Successively, a model of *frozen turbulence* may be applied: the target is expected to advect with the assumed mean velocity and the analysis can be focused on the kinematics relative to the mean field. We will refer to *global WBRRS* to denote the WBRRS for the whole grid.

For the curtain-leg layout it is convenient to further define a *local* (one per each grid column) WBRRS, as the orientation and geometry of the cells may vary from one to another. The origin of the local WBRRS is in the upper-left corner point of the generic cell, and moving with the assumed advection velocity. The x-axis is aligned along two consecutive grid corner points (ξ direction). The orientation of the remaining axes is set according to the characteristics of the flight and of the scanned surface. If the AC bank angle is limited ($\leq 5^\circ$), as in a slow coordinated turn, the scanned surfaces may be approximated by a horizontal (for HBDD) or an upright vertical surface (for VPDD). In this case, the y and z axes can be placed on a horizontal and a vertical plane respectively. If the scanned surface is more complex, the final orientation of the reference system is determined by imposing that the average direction between two consecutive corner-point columns (see

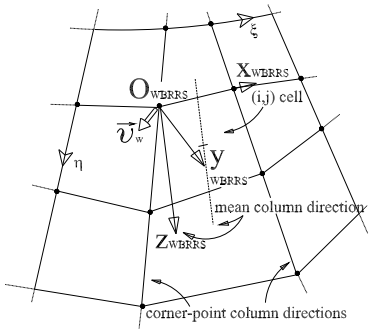

FIG. 5. Local Wind Based and Rotated Reference System (*local WBRRS*) for a curtain-leg VPDD. $\vec{v}_w$ is the grid advection velocity.

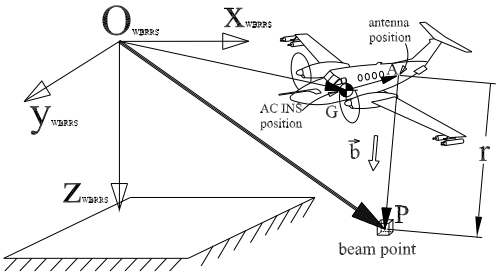

FIG. 6. Example of calculation of *beam point* coordinates. $\overrightarrow{OP} = \overrightarrow{OG} + \overrightarrow{GA} + r\,\vec{b}$. r is the range from the radar, G is the AC center of mass, A denotes the beam antenna position, and $\vec{b}$ is the beam unit vector.

Fig. 5) be contained in the final WBRRS xz (VPDD) or xy (HBDD) plane.

A (3×3) rotation matrix (RM2) (or an array of such matrices for curtain-leg cases) is defined as transformation matrix between UFRS and WBRRS (*local* WBRRS for curtain-leg cases). All the data, from distances and wind data to Doppler velocities, can then be mapped from the grid to the ground reference system. The grid points are also assigned latitude and longitude coordinates in order to refer the grid to a ground location. The grid origin can be adjusted to discard areas of the initial domain that, due to the fixed dual-beam geometry, are illuminated by only one beam.

3.1 *Straight-leg Grid*

Time integration of the AC air-relative velocity leads to the determination of the total length of the track (Λ) and of the mean course heading (defining the grid ξ direction) with respect to WBRRS. The length of the track, and the desired grid breadth (Ω) along η, are then divided according to a chosen number of cells N_ξ and N_η respectively, and to the desired spacing ratios (*HSR, VSR*). The (i,j)-th cell dimensions $\Delta\xi_i$ and $\Delta\eta_j$ along ξ and η, depend on the $(0,0)$-th cell size ($\Delta\xi_0$, $\Delta\eta_0$) as follows:

$$\begin{cases} \Delta\xi_i = (\mathrm{HSR})^i \cdot \Delta\xi_0 \\ \Delta\eta_j = (\mathrm{VSR})^j \cdot \Delta\eta_0 \end{cases} \tag{1}$$

The size of the $(0,0)$-th cell is determined according to Eq. (2):

$$\begin{cases} \Delta\xi_0 = \dfrac{\Lambda}{\sum_{k=0}^{N_\xi} \mathrm{HSR}^k} \\ \Delta\eta_0 = \dfrac{\Omega}{\sum_{l=0}^{N_\eta} \mathrm{VSR}^l} \end{cases} \tag{2}$$

The spacing ratios can be used to optimize the mesh density. From Eq. (1) it is straightforward to derive the WBRRS coordinates of the grid points. The origin $O(0,0,0)$ is identified with the upper-leftmost corner point. It is representative of the first position of the straight-pointing-beam antenna. The grid terminates with the last position of the straight-pointing beam antenna.

The radar data point (hereafter *'beam point'*) coordinates can be computed with respect to the WBRRS as illustrated in Fig. 6. For each beam, the pair ($prof$,r) identifies a point in space representative of a scatterer volume. Its coordinates can be calculated with simple vector geometry from the knowledge of the AC antenna positions and the beam unit vectors ($\vec{b}$).

3.2 *Curtain-leg Grid*

Analogously to the straight-leg case, AC INS and antenna positions are devised by time integration of the AC air-relative velocity. It is convenient to associate to the track 3-D spatial positions a curvilinear coordinate, s, i.e., the track length.

In order to derive the grid first row (closest to the AC) corner points, the track can be divided into arcs or chords (segments), see Fig. 7. Their length depends on the number of cells along ξ, on the stretching ratio HSR, and on the total length of the track. By adopting the segment subdivision the grid is regularized; however, with the arc (curvilinear) one, the number of radar profiles per grid cell, and therefore beam points, is kept near to uniform (or proportional to the cell size if HSR > 1).

In case of curvilinear subdivision of the track, the arc length ($\tilde{\Delta}\xi_i$) is determined by the first of Eq. (1), and each corner point along the track can thus be assigned an s coordinate. To obtain their WBRRS coordinates, the available straight-pointing beam antenna positions along the AC track, with their respective s, can be re-interpolated onto the newly calculated corner point s values.

If the track is divided into straight segments, their length ($\Delta\xi_i$) is still computed according to Eq. (1), but the corner point coordinates are calculated solving Eq. (3) following the geometry illustrated in Fig. 7.

$$\Delta\xi_i^2 = \|\overrightarrow{PQ}\|^2 + \Delta^2 - 2\|\overrightarrow{PQ}\|\,\Delta\,\overrightarrow{PQ}\cdot\hat{e}_s \tag{3}$$

In Eq. (3), P is the established $(i-1)$-th corner point (for i =1 it is the origin O), Δ is the unknown displacement along the $\hat{e}_s$ direction of $\tilde{Q}$ (the straight-pointing beam

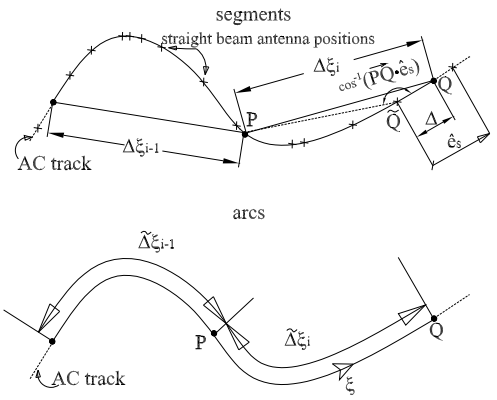

FIG. 7. The two options available to subdivide the track length for the grid first-row corner-point retrieval. Upper panel: chord subdivision option; bottom panel: arc subdivision option. P, Q are grid corner points; + symbols denote straight-pointing beam data points

point that minimizes the norm $\|\overrightarrow{P\tilde{Q}} - \Delta\xi_i\|$) needed to determine the next grid corner point Q; $\Delta\xi_i$ is the length of the i-th segment. Once the first-row corner points are calculated, they can be assigned a new s coordinate by simple re-interpolation.

The next step is to define all the other corner points in the normal-to-track direction (η). They are calculated following either the *local* straight-pointing beam direction or an Earth's strictly vertical (VPDD, WBRRS z-axis) or horizontal one (HBDD, WBRRS y-axis). To find the straight-pointing beam directions at the grid first-row corner points, an interpolation using the coordinate s and the beam unit vectors, known for all the recorded antenna positions, is employed. The η points are then easily determined by using the second of Eq. (1).

The coordinates of the beam points are calculated analogously to the straight-leg case.

4. VELOCITY RETRIEVAL

4.1 *Beam Point Assignment*

Once the grid is built, the beam points must be assigned to the grid cells in order to determine the velocity retrieval equations for each grid cell. Two different methodologies, though following the same principal, are applied for the straight and curtain-leg cases respectively. We will also assume that the allowed grid swath is limited to *SWTH* meters.

1) STRAIGHT-LEG CASES

The procedure is straightforward if a regularly spaced grid is adopted (i.e., if HSR $=$ VSR $=$ 1). The indices (i,j) of the cell to which a generic beam point $P(x,y,z) \in$ WBRRS (with $|z| < \frac{\text{SWTH}}{2}$) belongs, can be calculated using Eq. (4):

$$i = \text{floor}\left(\frac{x}{\Delta\xi_0}\right), \quad j = \text{floor}\left(\frac{y}{\Delta\eta_0}\right) \tag{4}$$

where 'floor' is the closest lesser integer of the argument. In Eq. (4), and in the previous swath inequality, a VPDD case is assumed; for HBDD y and z need be swapped.

For HSR,VSR $\neq$1, using Eq. (2), Eq. (4) rewrites:

$$\begin{cases} i = \text{ceil}\left\{\dfrac{\log\left(1 - x/\Delta\xi_0(1-\text{HSR})\right)}{\log \text{HSR}} - 1\right\} \\ j = \text{ceil}\left\{\dfrac{\log\left(1 - y/\Delta\eta_0(1-\text{VSR})\right)}{\log \text{VSR}} - 1\right\} \end{cases} \tag{5}$$

2) CURTAIN-LEG CASES

In the curtain-leg case, the assignment of beam points becomes more complicated due to the grid three-dimensionality. The search for the (i,j)-th cell containing the generic beam point $P(prof, r)$, associated with a curvilinear coordinate s, starts by calculating first estimates of the indices according to Eq. (6) for HSR, VSR =1. The more complex equations for non-unitary spacing ratios are omitted for sake of brevity.

$$\begin{cases} i_{\text{st}} = \text{floor}\left\{\dfrac{s}{\Delta\xi_0}\right\}, & j_{\text{st}} = \text{floor}\left\{\dfrac{r}{\Delta\eta_0}\right\} \\ i_{\text{sl}} = \text{floor}\left\{\dfrac{s + r\sin\iota}{\Delta\xi_0}\right\}, & j_{\text{sl}} = \text{floor}\left\{\dfrac{r\cos\iota}{\Delta\eta_0}\right\} \end{cases} \tag{6}$$

In Eq. (6) the subscripts 'st', 'sl' denote the relationships to adopt for straight-, slanted-pointing beam points; ι is the angle formed by the main beam directions.

The beam point coordinates are then checked against the boundaries of the found cell, based on the distance vector $\overrightarrow{OP}$ in the local WBRRS, and on the parameters SWTH, $\Delta\xi_i$, and $\Delta\eta_j$. Due to the potential skewness of the cells, *'cracks'* between them may exist. To minimize the loss of data points due to cracks, a limited overlap between contiguous cells can be allowed. If the point appears not to lie within the first located (i,j)-th cell, the search continues in the neighboring cells according to the interval defined by $[i - \text{tol}_i; j - \text{tol}_j] \times [i + \text{tol}_i; j + \text{tol}_j]$, where tol_i, tol_j are index tolerances. Their values can be assigned based on the maximum deviation of the AC attitude angles from their mean as in Eq. (7) for VPDD cases. The expressions for HBDD ones are analogous.

$$\begin{cases} \text{tol}_i = \text{ceil}\left\{r_{\text{max}}(\sin\left(\max|\theta - \bar{\theta}|\right)\cos\left(\max|\psi - \bar{\psi}|\right) \right. \\ \quad \left. + \sin\left(\max|\phi - \bar{\phi}|\right)\sin\left(\max|\psi - \bar{\psi}|\right))\Delta\xi_0^{-1}\right\} \\ \text{tol}_j = \text{ceil}\left\{r_{\text{max}}\left(1 - \cos\left(\max|\theta - \bar{\theta}|\right)\right.\right. \\ \quad \left.\left. \cdot\cos\left(\max|\phi - \bar{\phi}|\right)\right)\Delta\eta_0^{-1}\right\} \end{cases} \tag{7}$$

In the above equations the overbar denotes the flight-leg average, $\bar{\psi}$ is calculated in WBRRS, and r_{max} is the farthest rangegate from the AC; the 'ceil' function rounds up

the argument to the next closest integer and '$\max$' returns the maximum of the argument.

4.2 *Velocity Correction, Unfolding and External Wind Guess*

The AC motion has to be removed from the Doppler radial velocities so to attain the actual velocities (in UFRS) of the scatterers along the beam unit vectors. If the scatterer velocity exceeds the maximum Nyquist velocity (v_{nyq}), however, it will alias and fold within $(-v_{\text{nyq}}; v_{\text{nyq}}]$. Recentering the Nyquist interval about the mean wind speed along the radial direction often resolves the aliasing. It is assumed that the prescribed wind value does not change along the range, and that any folding is caused by the mean wind only. Under this hypothesis, even multiple folding can be resolved. The unfolding may not be successful if the folded velocities are affected by other phenomena, e.g., perturbations to the velocity field exceeding the unambiguous range such as strong shear, etc.

As mentioned in Section 2, an external estimate of the winds is necessary to derive a value of the cross-plane component. Beside the possibility of assigning a constant wind vector or the locally AC-measured winds or the Doppler retrieved average wind (consistent with what is chosen for the grid advection velocity, cf. Section 3), if the analysis is of the VPDD type, a vertical profile (*sounding*) of the wind velocity components in UFRS can be used. The sounding can come from an external source or can be defined following a turbulent boundary layer profile (e.g., *log-law* or *Ekman's profile*) by imposing that the flight level wind conditions be satisfied. The information about the ground elevation, necessary to devise the wind vertical profiles, can be determined from the records of the AC altimeter (altitude MSL) and those from the onboard radar altimeter, or from the radar nadir beam if the surface echo is available.

4.3 *Data Point Weighting*

The beam points belonging to the (i, j)-th cell are assigned weights according to one or two criteria based on the Inverse Distance Weighting (IDW), the Cressman Weighting Function (CSW) (Cressman 1959), the Exponential Weighting Function (EXW) (Mohr et al. 1986), and the Beam Skewness Weighting (BSW) method. In addition, data points can be weighted based on their returned power SNR level (Doviak and Zrnic 1993). The standard deviation of the mean Doppler velocity is a function of the SNR. For high SNR its minimum is bound by the spread of the spectrum due to the platform motion. At low SNR it saturates to the level of the receiver noise.

IDW. In the Inverse Distance Weighting, the weights are assigned to the beam points according to their distances from the centroid of the grid cell they belong to:

$$g_k = \frac{1}{(1 + d_k)^{c_{\text{idw}}}} \tag{8}$$

In Eq.(8), g_k is the weight for the k-th beam point, d_k its distance from the cell centroid, and c_{idw} the exponent of the IDW method, usually equal to 2.

EXW. The Exponential Weighting is expressed by:

$$g_k = \exp\left(\ln(c_{\text{exw}})\frac{d_k^2}{\text{ROI}^2}\right) \tag{9}$$

where c_{exw} is the value of the weight to be assigned to the k-th data point located at a distance d_k equal to the radius of influence ROI. Mohr et al. (1986) show that the ideal value for c_{gw} in the generalized Gaussian weighting function ($g_k = \exp[-d_k^2/c_{gw}^2]$) can be determined by $c_{gw} = 1.366\Delta$, where Δ is the spacing between input data. Assuming $c_{\text{exw}} = 0.1$ in Eq. (9) translates into an optimal value for ROI comparable to the coarsest spatial resolution in any grid direction. The radius of influence is usually set equal to the mean cell size, $(\Delta\xi_i + \Delta\eta_j)/2$.

CSW. The mathematical expression for the Cressman weighting is given by:

$$g_k = \begin{cases} \frac{\text{ROI}^2 - d_k^2}{\text{ROI}^2 + d_k^2} & \text{if } d_k \leq \text{ROI}, \\ 0 & \text{if } d_k > \text{ROI}. \end{cases} \tag{10}$$

BSW. The Beam Skewness Weighting is based on the component normal to the sought scanning plane of the beam unit vector associated with the beam point. In case of straight-leg, the desired scanning plane is either vertical (VPDD, WBRRS xz) or horizontal (HBDD, WBRRS xy). For curtain-leg cases, the reference plane is determined by the *local* WBRRS xz (VPDD) or xy (HBDD) plane. Eq. (8) can then be used to calculate the weights interpreting d_k as the absolute value of the component of the beam-unit-vector normal to the reference plane.

4.4 *Velocity Inverse Decomposition Problem*

The velocity $\vec{v}$ associated with the mean motion of the scatterers in the (i, j)-th cell is calculated by solving the following linear system of equations:

$$\vec{v} \cdot \vec{b}_k = \mathsf{v}_k, \quad k = 1 \ldots m \tag{11}$$

where '$\cdot$' indicates a dot-product, $\vec{b}_k$ are the beam unit vectors associated with the m beam points lying within the grid (i, j)-th cell, and v_k are the corresponding Doppler radial velocities (corrected for AC motion). In system (11) the weights g_k have been implicitly included in the variables, so that each k-th equation needs to be thought as multiplied by the relative weight g_k.

v_x, v_y, and v_z are the unknown velocity components along the axes of WBRRS. However, $\vec{v}$ is the mean velocity calculated with respect to UFRS. At a later stage, as already stated, it may be convenient to remove the mean wind (advection) velocity in order to investigate the air-relative kinematic field. System (11) re-writes in matrix format:

$$\begin{bmatrix} b_{11} & b_{12} & b_{13} \\ b_{21} & b_{22} & b_{23} \\ \vdots & \vdots & \vdots \\ b_{m1} & b_{m2} & b_{m3} \end{bmatrix} \begin{Bmatrix} v_x \\ v_y \\ v_z \end{Bmatrix} = \begin{Bmatrix} \mathsf{v}_1 \\ \mathsf{v}_2 \\ \vdots \\ \mathsf{v}_m \end{Bmatrix} \tag{12}$$

The number of points in each cell, m, may be less, equal or greater than three (i.e., the number of unknowns). It follows that the matrix $[B]$, first matrix in Eq. (12), could have a gamut of rank values with upper bound equal to $\min(m, 3)$. Thus the system $[B]\vec{v} = \underline{v}$, that can be interpreted as mapping function $\mathcal{F}$ between the hyperspaces $\mathcal{S}(\vec{v}) \in \mathbb{R}^3$ and $\mathcal{S}(\underline{v}) \in \mathbb{R}^m$, might result *under-* or *overdetermined*. In addition, if the matrix rank is less than $\min(m, 3)$ the matrix and the system in Eq. (12) are said to be *rank deficient*.

Due to the nature of the information collected, the system should be characterized by an effective rank less than three. Errors in the $[B]$ entries might yield a matrix rank greater than what it should effectively be. Small deviations in the aircraft attitude angles, for instance, can cause limited non-collinearity among the beam directions. It is to be expected, however, that all the data points will carry velocity information along various radial directions not strongly independent from just two. The latter are associated with the installation slanted and straight-pointing beam unit vectors. Hence, the possibility of finding a well-conditioned full rank-3 system is minimal. In most cases the rank will be two, being one if data from one of the two beams are missing or discarded.

The space of the solution, or the *range* of $\mathcal{F}$, $\mathcal{S}_R(\underline{v})$, is the subspace of $\mathcal{S}(\underline{v})$ which can be mapped by $[B]$, of dimension equal to the rank of $[B]$. If $[B]$ is rank deficient, the subspace of $\mathcal{S}(\vec{v})$ mapped by $[B]$ into $[0]$ ($\in \mathbb{R}^m$) is called *null-space* ($\mathcal{S}_0(\vec{v})$), and has dimension equal to $3 - \mathrm{rank}\,[B]$.

System (12) can be solved in a *least-squares* sense by minimizing the *residual* norm, $\|\underline{\mu}\| = \|[B]\vec{v} - \underline{v}\|$. This can be accomplished by finding the so-called *pseudo-inverse* matrix $[B^+]$. It can be proven that if $[B^+]$ satisfies the *Moore-Penrose* conditions (Golub and Van Loan 1989), then the least-squares solution is $\vec{v}_{\mathrm{LS}} = [B^+]\underline{v}$. In case of underdetermined or rank-deficient systems there are an infinite number of solutions. Uniqueness can be regained by searching for the solution of minimum norm.

A powerful method for solving the described type of system is the *singular value decomposition method (SVD)* (Golub and Van Loan 1989). An $(m \times 3)$ matrix $[B]$ can be decomposed via SVD as follows:

$$[B] = [U][W][V]^T \tag{13}$$

where $[U]$ is an $(m \times 3)$ orthogonal matrix, $[W]$ is (3×3) diagonal matrix of singular values and $[V]$ is a (3×3) orthonormal matrix. The SVD readily provides the *condition number* κ_{svd} of the rectangular matrix $[B]$:

$$\kappa_{\mathrm{svd}}([B]) = \frac{\varsigma_{\mathrm{max}}([B])}{\varsigma_{\mathrm{min}}([B])} \tag{14}$$

where $\varsigma_{\mathrm{max}}([B])$ and $\varsigma_{\mathrm{min}}([B])$ are the maximum and minimum singular values of $[B]$. Eq. (14) is strictly valid for full-rank matrices. In this case, the sensitivity of the least-squares solution and of its residual to perturbations (errors) in the data ($[B]$ and $\underline{v}$) is of the order of κ^2_{svd} and κ_{svd} respectively (Golub and Van Loan 1989). The larger the matrix condition number the more *ill-conditioned* the problem. The smallest singular value denotes the 2-norm distance of $[B]$ from the set of all rank-deficient matrices. If κ_{svd} is infinity then $[B]$ is singular (rank deficient) and the uncertainties associated with the least-squares solution are hardly predictable for it being not even a continuous function of the data (Golub and Van Loan 1989). If the system is underdetermined, the uncertainty in the solution due to errors in the data is of order κ_{svd}.

The pseudo-inverse matrix $[B^+]$ can be expressed via SVD decomposition as follows:

$$[B^+] = \left([U][W][V]^T\right)^{-1} = [V][W]^{-1}[U]^T \tag{15}$$

with $[W]^{-1}$ being a diagonal matrix $[W]^{-1} = \mathrm{diag}\left[\frac{1}{\varsigma_{ii}}\right]$, where ς_{ii} are the singular values of $[B]$, and $\mathrm{w}_{ii} = 1/\varsigma_{ii}$ is replaced by 0 if $\varsigma_{ii} = 0$.

In order to improve the *condition-status* of the matrix, a cutoff value is adopted by rejecting those singular values below a prescribed threshold (usually based on the ratio to the maximum singular value < 0.01), thus replacing their reciprocals with 0 in $[W]^{-1}$. Such an event is expected to occur in the positions corresponding to the *cross-plane* component of the velocity. In other words, a very low singular value is expected associated with the second (third) component of the velocity not lying in the expected VPDD (HBDD) scanning plane. An important property of the SVD decomposition is that the columns of $[U]$, whose same-numbered elements w_{ii} are non-zero, represent an orthonormal set of basis vectors spanning $\mathcal{S}_R(\underline{v})$, i.e., the range. The *sum of squares* (square of the residual norm) can then be expressed as (Golub and Van Loan 1989):

$$\underline{\mu}^T\underline{\mu} = \underline{v}^T\underline{v} - \sum_{j=1}^{\hat{k}} \left([U]^T\underline{v}\right)_j^2 \tag{16}$$

If the first $\hat{k}$ components (*principal components*) corresponding to the largest singular values are, in fact, those responsible for reducing the sum of squares, the problem has a solution safely computed by leaving out the remaining components (i.e., those corresponding to small singular values, conditionally set to 0). If this were not the case, or in other words if $\underline{v}$ were best approximated by columns of $[U]$ corresponding to small singular values, then the problem would be ill-conditioned.

The SVD solution of the linear system in (12) can then write:

$$\vec{v} = \left([V][W]^{-1}[U]^T\right)\underline{v} \tag{17}$$

If the system is overdetermined then the solution has the property of minimizing the residual in the least-squares sense. In the case of an underdetermined or rank-deficient system, it minimizes the residual and has the minimum norm among all possible minimizers (Golub and Van Loan 1989).

The columns of $[V]$, whose same-numbered elements w_{ii} are zero, constitute an orthonormal set of basis vectors spanning $\mathcal{S}_0(\vec{v})$, i.e., the null-space. The null-space,

in the dual-Doppler analysis with rank=2, can be represented by a unit vector, i.e., the *normal* to the *solution plane*. The latter identifies, from a geometrical point of view, the best-fit, in the least-squares sense, of all the planes determined by the beam unit vector pairs. Mathematically it is $\mathcal{S}_R(\underline{\mathsf{v}})$.

Adding an arbitrary linear combination of the null space basis to the solution will still satisfy the least-squares problem (12). This can be advantageously used to add the external wind information to the solution and obtain a three-dimensional wind calculation for every grid cell. More importantly, the external information upon the winds allows for the quantification of the cross-plane component. By accounting for the latter, the eventual error committed by transferring the calculated velocity vector from the solution plane onto the reference plane (for instance a vertical one in case of VPDD) is minimized.

The availability of the null-space basis allows to calculate how far the plane of reference is from the actual solution plane. An analysis of the angles determined by the normals to the cited planes can aid in the assessment of the performance of the dual-Doppler retrieval.

5. SOURCES OF ERROR IN THE ANALYSIS

There is a number of error sources in a multiple Doppler analysis, especially if based on an airborne platform. The errors depend on the radar characteristics, its processor design and on the data collection process. Specific aspects of the atmospheric nature of the target further affect the errors, from the broadening of the Doppler power spectrum to the temporal uncertainties due to the target advection in the time interval between scans. In this section, we address the main sources of error thus to offer confidence intervals depending on the target under investigation and the environmental conditions.

The absolute velocity $\vec{v}_P^a$ of a scatterer occupying a point (volume) P in space can be decomposed as:

$$\vec{v}_P^a = \vec{v}_P^{rel} + \vec{v}_P^{tr} = \vec{v}_P^{rel} + \vec{v}_\mathsf{G} + \vec{\omega} \wedge \overrightarrow{\mathsf{G}P} \qquad (18)$$

where $\vec{v}_P^{rel}$ is the scatterer velocity relative to the moving platform frame (i.e., ACRS) and $\vec{v}_P^{tr}$ is its velocity if considered fixed with respect to that frame; $\vec{v}_\mathsf{G}$ is the velocity of the AC center of mass (G); the velocity due to the motion about G is given as cross-product of the frame rotational velocity $\vec{\omega}$ and distance vector $\overrightarrow{\mathsf{G}P}$. By decomposing Eq. (18) along a beam direction $\vec{b}$, the radial velocity (v) is obtained:

$$\mathsf{v} = \vec{v}_P^a \cdot \vec{b} = \vec{v}_P^{rel} \cdot \vec{b} + \vec{v}_P^{tr} \cdot \vec{b} \qquad (19)$$

The uncertainties affecting v are due to: errors in the beam pointing angles ($\vec{b}$), errors in the calculated AC ground velocity (INS/GPS system errors) affecting $\vec{v}_P^{tr}$, and errors in the radar retrieval of $\vec{v}_P^{rel} \cdot \vec{b}$.

Beside those directly affecting the measured radial velocities, other error sources will affect the dual-Doppler derived 2-D velocity vector. They include uncertainties in the assumption of the wind 'cross-plane component', target advection and evolution effects, grid orientation and target visualization distortion. All are discussed in the following sections.

5.1 *Errors in the platform motion affecting the grid*

The knowledge of the aircraft position and velocity vector is subject to instrumental errors. Although care is taken to remove Schuler oscillations in the INS, and a baro-inertial loop algorithm is employed to reduce the uncertainty in the ground vertical velocity, errors in the AC position and its velocity with respect to the Earth's coordinate system need be considered. In Table 2, the accuracy of the basic UWKA instrumental suite is reported (cf. , Brown (1993) and `http://flights.uwyo.edu/bulletin1.html`).

The AC position error is relevant in case the data have to be compared to ground radar data. The error in the AC ground velocity is more important as it propagates into the grid construction, the Doppler velocity correction (AC motion removal), and into the estimate of the wind in proximity of the target.

The air velocity is calculated by means of a gust probe, i.e., a differential 5-hole pitot tube mounted on the forward AC boom (Brown 1993), and of the data provided by the INS and GPS. The measurement accuracy is estimated to be affected by a random error of 0.4 m s^{-1} and a systematic error of usually less than 0.4 m s^{-1}. Since the grid is built following the aircraft in an air-relative frame, the error translates into the calculation errors of the UWKA air-relative velocity and thus into the orientation of the grid and into a distorted visualization of the target structures. The same error arises from an incorrect choice of the advection velocity for the grid. In addition, if shear is present, the target may not move at the same speed everywhere, thence the grid will distort the target properties at least in some sectors. This is difficult to quantify since a knowledge of the environmental conditions is often incomplete. A way to reduce the errors in case of significant shear is to adopt the curtain-leg grid construction and imposing a variable advection velocity, function of the position along the track.

Conservatively assuming an error for the AC ground velocity and air velocity on the order of 1 m s^{-1}, the error in the horizontal components of the air-relative AC velocity is approximated by $\sqrt{2}$ m s^{-1}. This causes a distortion of the grid cells proportional to the ratio of the estimated to the actual velocity. For the typical UWKA air speed of $\sim$90 m s^{-1} the distortion is on the order of 2%. The associated relative error in the gradient of a generic quantity along ξ can be calculated to be lower than 2.2%.

The relative error in the estimated grid orientation writes:

$$\varepsilon_\xi^{rel} = \frac{\arctan \frac{v_{\mathsf{AC}x} + \varepsilon_{v_{\mathsf{AC}x}}}{v_{\mathsf{AC}y} + \varepsilon_{v_{\mathsf{AC}y}}}}{\arctan \frac{v_{\mathsf{AC}x}}{v_{\mathsf{AC}y}}} - 1 \qquad (20)$$

where $v_{\mathsf{AC}x}$, $v_{\mathsf{AC}y}$ are the east, north component of the AC air-relative velocity and $\varepsilon_{v_{\mathsf{AC}x}}$, $\varepsilon_{v_{\mathsf{AC}y}}$ their errors. The effective absolute error is less than 1.5° for typical flight

Parameter	Instrument	Random Error	Bias	95% uncertainty
Pressure Altitude	Rosemount HADS	0.25 mbar	—	0.5 mbar
Lat./long. (INS)	Honeywell Laseref SM	0.8 mm h^{-1}	—	1.66 mm h^{-1}
Lat./long. (GPS)	Trimble 2000	12 m	—	25 m
Ground velocity	Honeywell Laseref SM	0.343 m s^{-1}	—	0.685 m s^{-1}
Vertical velocity	Honeywell Laseref SM	0.0762 m s^{-1}	—	0.152 m s^{-1}
Pitch/Roll angle	Honeywell Laseref SM	0.025°	0.1°	0.111°
Yaw angle	Honeywell Laseref SM	0.1°	0.071°	0.212°
Sideslip	radome air motion syst.	0.0253°	0.0872°	0.096°

Table 2. Instrument uncertainty for the UWKA basic instruments. The uncertainty is calculated as the root-sum-square of the bias and random error at the 95% (2 std.dev.) confidence level.

speeds.

These are minor uncertainties and should not prevent a good application of the analysis technique.

5.2 *Errors in the Radial Velocity Due to Uncertainties in the Platform Motion and Beam Pointing Angles*

As stated, errors in the INS/GPS-measured ground velocity further affect the calculation of the corrected (absolute) Doppler radial velocity. The INS/GPS system, in fact, retrieves $\vec{v}_P^{tr}$ (cf. Eq. (19)), thus the errors from the latter directly propagate into v.

The beam unit vectors are determined via a procedure that minimizes the ground echo mean Doppler velocity and its standard deviation, which ideally should be null. Obviously, the INS/GPS errors will interfere with this calculation. Uncertainties in the beam unit vectors also arise from problems inherent in the ground echo identification, due to the receiver finite filter response, beam filling effects and potential asynchronization between AC and radar data. Beside the way the beam retrieval procedure is carried out, random errors may also arise due to aircraft frame bending and twist. These effects should be of less concern in a compact airframe such as the non-slender UWKA one.

On the basis of a series of calibration flights, we claim a maximum standard deviation in the directional cosines < 0.01, corresponding to the angle errors reported in Table 3 for the UWKA installation. Following Fig. 5.2, we can calculate the radial velocity error, $\varepsilon_{\mathrm{v},1}$, due to a wrong assumption of the beam unit vector and platform motion.

The actual radial velocity along the assumed beam unit vector, $\vec{b}_a$, is: $\mathrm{v}_{b_a} = \frac{\mathrm{v}}{\cos\delta_b} - k_{\mathrm{v},x}\, r\, \delta_b$, where v is the true absolute scatterer velocity along $\vec{b}$, $k_{\mathrm{v},x}$ the shear across the beam of the radial velocity along $\vec{b}_a$; r is the range of the scatterer, and δ_b the angle between $\vec{b}_a$ and the actual beam direction $\vec{b}$.

The error $\varepsilon_{\mathrm{v},1}$ can then be expressed as the difference

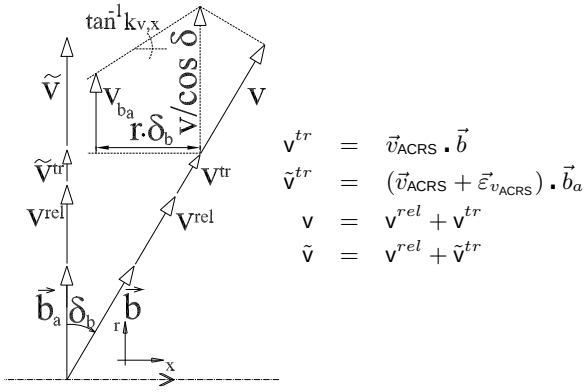

FIG. 8. Radial velocity error contributions by AC motion and beam direction uncertainties. $\vec{b}$ and $\vec{b}_a$ are the actual and assumed beam orientations respectively, δ_b the angle between them. $\vec{\varepsilon}_{v_{\mathrm{ACRS}}}$ is the error in the platform ground velocity $\vec{v}_{\mathrm{ACRS}}$ (including the contribution due to the rotation about the AC G); r is the target range. More in text.

between v_{b_a} and the assumed radial velocity ($\tilde{\mathrm{v}}$) along $\vec{b}_a$:

$$\varepsilon_{\mathrm{v},1} = \mathrm{v}_{b_a} - \tilde{\mathrm{v}} = \mathrm{v}^{rel}\left[1 - \frac{1}{\cos\delta_b}\right] + (\vec{v}_{\mathrm{ACRS}} + \vec{\varepsilon}_{v_{\mathrm{ACRS}}}) \cdot \vec{b}_a - \frac{\vec{v}_{\mathrm{ACRS}} \cdot \vec{b}}{\cos\delta_b} + k_{\mathrm{v},x}\, r\, \delta_b \quad (21)$$

Assuming $\delta_b \to 0$, Eq. (21) can be approximated at the first order by:

$$\varepsilon_{\mathrm{v},1} = \left[\vec{v}_{\mathrm{ACRS}} \cdot (\vec{b}_a - \vec{b}) + \vec{\varepsilon}_{v_{\mathrm{ACRS}}} \cdot \vec{b}_a\right] + k_{\mathrm{v},x}\, r\, \delta_b \quad (22)$$

The terms in the brackets represent the errors associated with the misrepresentation of the platform motion contribution, whilst the term containing $k_{\mathrm{v},x}$ is the error due to the spatial misplacement of the scatterer velocity. Eq. (22) is a weak function of the attitude of the aircraft and thus of the cross-wind component and vertical velocity of the aircraft, with variations in the errors less than 0.1 m s^{-1} for typical flight envelopes. In Table 4, ranges for the bracketed term in Eq. (22) are offered for a situation with horizontal air-speed equal to 90 m s^{-1}, a vertical

antenna	$\arccos(b \cdot \hat{e}_x)$		$\arccos(b \cdot \hat{e}_y)$		$\arccos(b \cdot \hat{e}_z)$		$\delta_{b\,\max}$
(units: degree)	mean	std. dev.	mean	std. dev.	mean	std. dev.	
nadir	93.180	0.058	89.890	0.391	3.204	0.077	1.114
dwn-fwd	63.845	0.087	89.649	0.526	26.164	0.090	2.992
side	90.700	0.091	0.783	0.236	89.818	0.358	0.960
side-fwd	53.716	0.324	36.337	0.317	88.618	1.031	6.337

Table 3. UWKA WCR antenna beam mean and standard deviation angles with respect to ACRS axes. $\delta_{b\,\max}$ are maximum departure angles from the actual beam unit vectors.

	nadir	nadir-fwd	side	side-fwd
$\varepsilon_{v,1}$ range (m s^{-1})	0.565-0.768	0.286-0.993	0.669-0.767	0.368-1.373

Table 4. Radial velocity errors due to misrepresentation of the AC motion along the beam direction. Adopted assumptions in text.

velocity of about 6 m s^{-1}, a cross-wind of 10 m s^{-1}, and $\vec{\varepsilon}_{v_{\text{ACRS}}}$ with components along the ACRS axes of magnitude equal to $\sqrt{3}/3$. The results are based on the uncertainties given in Table 3.

5.3 *Beam Reciprocal Misalignment*

Under certain flight conditions the dual-Doppler beams may not be oriented in the plane described by the aircraft track and the normal to it. If a sideslip angle β exists, for instance, the nadir and nadir-forward beam would not belong to the vertical plane of the air-relative track. The sideslip is usually limited as the aircraft flies a Lagrangian trajectory. An analogous error would occur for the HBDD beams in case an unusual angle of attack α were maintained for an extended period of time. The lateral pointing antennas are mounted so to scan a horizontal plane in straight and leveled flight with the usual trim pitch of the UWKA ($\sim$3.5° for the typical cruise speed and take-off weight). Situations in which a departure from the trim condition might occur include pilot's decisions to force certain aircraft attitudes to keep a recommended air-speed (different from the cruise one) or to keep a prescribed ground track. Transient responses to gusts and the potential presence of shear should also be taken into account. Auto-pilot or stability-augmentation-systems are generally employed reducing both the overshoot and the time to steady-state for the motion oscillations following gust disturbances.

For typical research flights we have measured sideslip (angle of attack change) standard deviations on the order of 0.5° (1°) and maximum deviations from trim conditions (i.e., $\bar{\beta}$ =0°, $\bar{\alpha}$ =3.5°) on the order of 3.5° (2°). The transverse distance between data points with respect to the reference plane of scan is given by $\Delta_\beta = r b_{\text{sl}_x} \sin\beta$, where b_{sl_x} is the direction cosine of the slanted-pointing beam along the ACRS x-axis (the change in α replaces β for HBDD). For a range of r =3 km the transverse distances associated with the reported standard deviation (maximum) of the aerodynamic flow angles are: $\Delta_\beta \approx$11.5 m (81 m) and $\Delta_\alpha \approx$31 m (62 m). Assuming a cross-track radial velocity gradient on the order of k_v =0.005 s^{-1}, the maximum values for the error in the assumed *slanted-pointing beam velocity* due to the data point displacement, $\varepsilon_{v,2}$, is $\sim$0.4 m s^{-1} and $\sim$0.3 m s^{-1} for the nadir-forward and side-forward antennas respectively.

The grid swath may be chosen small enough to naturally exclude from the analysis the points affected by such errors. However, at large ranges the radar resolution is degraded due to the larger beam resolution volume (at 3 km range the characteristic transverse size is $\sim$40 m for a 0.76° half-power beamwidth). Thence, the above calculated displacement effect is somewhat mitigated as the Doppler velocity is weighted over a larger volume. It is then reasonable to initially choose a swath large enough to contain these points and to allow a coarser grid resolution at larger ranges to account for this and other effects (cf. Section 5.8).

If wind shear perpendicular to the reference plane is present, even in the case of null sideslip (or null α'), a virtual offset between the surfaces described by the two beams exists. Assuming again k_v as the vertical (or horizontal for HBDD) shear magnitude, the effective sideslip (or angle of attack deviation) is approximated by $\beta_{\text{eff}} = \beta + \arctan\left(\frac{k_v\, r}{v_{\text{AC}}}\right)$, where v_{AC} is the AC airspeed (with α' replacing β for HBDD). For $k_v \simeq$0.005 s^{-1}, v_{AC} =90 m s^{-1} and r =3 km, the contribution to the effective sideslip from the ambient shear is $\sim$9.5°. The error in the slanted-pointing beam Doppler velocity could thus be substantial if the shear in the radial velocity along the grid transverse direction were significant.

The importance of selecting an appropriate value for the grid swath becomes evident. Not only does it determine the number of points accepted in the grid cell, but it plays a role in the grid filtering of the target features as well. Too small a swath would cause very few point to participate in the inverse decomposition solution system, producing errors related to the scarcity of the samples within the grid cell. Contrarily, too large a swath might introduce errors because of the shear across the grid plane, i.e., the three-dimensionality of the flow might affect the results in the sought 2-D field. It is then a trade-off between a finer resolution and a coarser one characterized by reduced errors, which needs to be assessed based on an *a-priori* knowledge of the background flow properties.

5.4 *Errors due to the Estimate of the Cross-Plane Component*

Errors in the estimate of the mean ambient wind propagate from those of the INS/GPS and gust-probe instruments. These errors will contaminate the 'cross-plane component' of the wind velocity, which is necessary for an accurate dual-Doppler 2-D retrieval (cf. Section 4.4). Unaccounted significant shear in this component across the grid can further affect the results. Generally, the errors are expected to be larger for VPDD analyses than for HBDD ones due to the nature of the atmospheric shear.

An estimate of these errors in the final kinematic field can be attained assuming an error for the assumed wind velocity and an angle between solution and reference planes (cf. Section 4.4). The departure from the reference plane can be approximated based on the standard deviations of the AC attitude angles for a typical dual-Doppler flight leg. Referring to a straight and level flight attitude, the angle γ_{err} between the reference and the actual plane of scan writes for VPDD and HBDD as:

$$\begin{cases} \gamma_{\text{err}}^{\text{VPDD}} = \arccos\left(\cos\sigma_\phi \cos\sigma_\psi\right) \\ \gamma_{\text{err}}^{\text{HBDD}} = \arccos\left(\cos\sigma_\theta \cos\sigma_\phi\right) \end{cases} \tag{23}$$

If $\sigma_\theta = \sigma_\phi = \sigma_\psi$ =3° (standard deviations in pitch, roll and yaw), Eq. (23) yields: γ_{err} =4.24°. Defining $\vec{\varepsilon}_{\text{w}}$ as the error in the external estimate of the wind (including the effects of unaccounted shear throughout the grid domain and errors in the ambient wind measurement), its component along the normal ($\vec{n}_{\text{LS}}$) to the solution plane (i.e., the cross-plane component) writes:

$$\begin{cases} \vec{\varepsilon}_{\text{w}} \cdot \vec{n}_{\text{LS}} = \varepsilon_{\text{xp}}^{\text{VPDD}} = \\ -\varepsilon_{\text{w}_x} \cos\sigma_\phi \sin\sigma_\psi + \varepsilon_{\text{w}_y} \cos\sigma_\phi \cos\sigma_\psi + \varepsilon_{\text{w}_z} \sin\sigma_\phi \\ \vec{\varepsilon}_{\text{w}} \cdot \vec{n}_{\text{LS}} = \varepsilon_{\text{xp}}^{\text{HBDD}} = \\ \qquad = \varepsilon_{\text{w}_x} \left(\sin\sigma_\theta \cos\sigma_\psi + \cos\sigma_\theta \sin\sigma_\phi \sin\sigma_\psi\right) + \\ \qquad + \varepsilon_{\text{w}_y} \left(\sin\sigma_\theta \sin\sigma_\psi - \cos\sigma_\theta \sin\sigma_\phi \cos\sigma_\psi\right) + \\ \qquad + \varepsilon_{\text{w}_z} \cos\sigma_\theta \cos\sigma_\phi \end{cases} \tag{24}$$

Decomposing the errors in Eq. (24) along ξ and η directions, one obtains:

$$\begin{cases} \varepsilon_{\text{xp}_\xi}^{\text{VPDD}} = \varepsilon_{\text{xp}}^{\text{VPDD}} \cos\sigma_\phi \sin\sigma_\psi \\ \varepsilon_{\text{xp}_\eta}^{\text{VPDD}} = \varepsilon_{\text{xp}}^{\text{VPDD}} \sin\sigma_\phi \\ \varepsilon_{\text{xp}_\xi}^{\text{HBDD}} = \varepsilon_{\text{xp}}^{\text{HBDD}} \left(\sin\sigma_\theta \cos\sigma_\psi + \cos\sigma_\theta \sin\sigma_\phi \sin\sigma_\psi\right) \\ \varepsilon_{\text{xp}_\eta}^{\text{HBDD}} = \varepsilon_{\text{xp}}^{\text{HBDD}} \left(\sin\sigma_\theta \sin\sigma_\psi - \cos\sigma_\theta \sin\sigma_\phi \cos\sigma_\psi\right) \end{cases} \tag{25}$$

Adopting the above values for the attitude standard deviations, and $\|\vec{\varepsilon}_{\text{w}}\|$ =5 m s^{-1}, the errors amount to: $\varepsilon_{\text{xp}_\xi} \simeq \varepsilon_{\text{xp}_\eta} \simeq 0.17$ and 0.18 m s^{-1} for VPDD and HBDD respectively. For $\sigma_\phi \simeq$5°, the errors along the η direction would become ∼0.28 and 0.29 m s^{-1}, for VPDD and HBDD respectively.

Note that $\varepsilon_{\text{xp}_\xi}$ and $\varepsilon_{\text{xp}_\eta}$ would sum to the errors deriving from the estimate of the mean translational wind, in case the final 2-D kinematic field is then calculated relative to the moving frame, i.e., in a *storm-relative* reference.

5.5 *Liquid water Attenuation, Side-Lobe and Transmitter Leakage Effects*

If shear in the radial velocity is significant within the pulse volume, attenuation of reflectivity due to liquid water content can produce an altered measurement of the mean Doppler velocity. Uncertainties on the order of 1 m s^{-1} for an airborne X-band radar have been reported (Hildebrand and Mueller 1985). These effects are hardly generalized as they depend on the radar configuration and the beam shape, but at W-band attenuation is certainly important (Lopez et al. 2000; Vali and Haimov 2001). Considering a simplified scenario with backscattering cross-section per unit volume (i.e., *reflectivity*), $\varrho(r)$, decreasing function of the range r, and assuming an attenuation factor $K_\varrho(r)$ (dB km^{-1}), the radial velocity measured at range r =$\hat{r}$ is given by:

$$\tilde{\mathsf{v}}(\hat{r}) = \frac{\int_{r_1}^{r_2} \tilde{\varrho}(r)\mathsf{v}(r)dr}{\int_{r_1}^{r_2} \tilde{\varrho}(r)dr} \tag{26}$$

where $\mathsf{v}(r) = \mathsf{v}(r_1) + k_{\mathsf{v}}(r - r_1)$ is the radial velocity assumed to undergo a linear shear (k_{v}, s^{-1}) in the radial direction, $\tilde{\varrho}(r)$ is the 'attenuated' reflectivity profile along the range, and r_1, r_2 are the minimum, maximum radial distance within the pulse volume. The original backscattering coefficient can be expressed as a function of the range and of a gradient k_ϱ (m^{-2}): $\varrho(r) = \varrho(r_1) + k_\varrho\,(r - r_1)$. Assuming a linear increase of the liquid water content with the range, the attenuation coefficient becomes: $K_\varrho(r) = K_{\varrho_0}\left[1 + k_{\text{lwc}}(r - r_1)\right]$, where K_{ϱ_0} is the value of the attenuation coefficient at r =r_1, and k_{lwc} is the rate of the (dimensionless, i.e., per g m^{-3}) liquid water content along the radial directions in m^{-1} The attenuated volumetric backscattering cross-section profile can then write: $\tilde{\varrho}(r) = \varrho(r)\, 10^{\frac{-K_{\varrho_0}(r-r_1)}{10}\left(1+\frac{k_{\text{lwc}}(r-r_1)}{2}\right)}$.

The radial velocity measured in absence of attenuation can be obtained using Eq. (26) by setting $K_\varrho \equiv$0. By subtracting the attenuation affected velocity from the latter, and carrying out the extensive algebra yields the error in the radial velocity. A further simplified model to estimate the maximum effect of attenuation consists of concentrating the scatterers in two point locations across the pulse volume, i.e., at r_1 and r_2.

$$\varepsilon_{\mathsf{v},3} = \left|\frac{\varrho_1(\varrho_1 + k_\varrho r_s)k_{\mathsf{v}} r_s(q-1)}{2\varrho_1^2(q+1) + \varrho_1 k_\varrho r_s(3q+1) + (r_s k_\varrho)^2 q}\right| \tag{27}$$

where $r_s = r_2 - r_1$ is the rangegate spacing, $q = 10^{\frac{-K_{\varrho_0} r_s}{10}(1+\frac{k_{\text{lwc}} r_s}{2})}$. Note that due to the chosen $\tilde{\varrho}(r)$ function, weighting the velocities more at closer than farther ranges with respect to $\varrho(r)$, the 2-point approximation is a conservative estimate of the error that would be calculated using the integral forms in Eq. (26).

$\varepsilon_{\mathsf{v},3}$ is a function of the gate size weakly dependent on the reflectivity at range $\hat{r}$. If the liquid water content,

true reflectivity (ϱ) and radial velocity are assumed to vary linearly along the range with rates equal to .002 gm^{-2}, -40 dB km^{-1}, and 0.5 s^{-1} respectively, the maximum absolute error in the radial velocity is less than 0.15 m s^{-1} for rangegate sizes $<$80 m and reflectivity between -40 and 40 dBZ. The variable rates are conservative estimates even for extreme cumulus convection regimes.

Attenuation effects may play a further role in the beam point SNR-weighting within the grid cell. At typical grid resolutions on the order of the rangegate size, however, the effect will again be negligible.

Side-lobe effects can also contribute to radial velocity errors in case large gradients in reflectivity and velocity are present. An approximate expression for the absolute error is given by:

$$\varepsilon_{\mathrm{v},4} = \left| \frac{k_{\mathrm{v},x}\, r\, \delta_l (\varrho + k_{\varrho,x} r\, \delta_l)\, 10^{-K_l/10}}{\varrho + 10^{-K_l/10}(\varrho + k_{\varrho,x} r\, \delta_l)} \right| \tag{28}$$

In Eq. (28) K_l, δ_l are the side-lobe power and orientation angle relative to the main lobe (respectively $K_l \approx$-20 dB and $\delta_l \approx 2^\circ$ for the WCR antennas); the reflectivity and radial velocity are thought to vary linearly in the across-beam direction with gradients $k_{\varrho,x}$ and $k_{\mathrm{v},x}$ respectively, and ϱ is the main lobe reflectivity at range r. It can be derived by calculating the difference between the measured radial velocity (affected by sidelobing) and the one that would be measured in absence of side-lobes. The former is calculated, at a first order approximation, as the reflectivity-weighted velocity between those relative to the main and first sidelobe.

Even for the extreme simultaneous occurrence of a 0.005 s^{-1} shear and a 0.04 dBZm^{-1} reflectivity gradient, the errors are below 0.3 m s^{-1} for ranges ≤ 3 km and SNR ≥ -5 dB, and below 0.2 m s^{-1} for SNR ≥ 0 dB.

5.6 *Random Errors related to the Finite Resolution Volume*

For weather targets, attention must be paid to the effects of the *pulse-volume filtering*. The adopted radial velocity, is the mean of the Doppler power density spectrum associated with the distribution of the radial velocities of the scatterers within the pulse volume (Doviak and Zrnic 1993). This translates into the convolution of the reflectivity-weighted velocities with the beam illumination function (Srivastava and Atlas 1974; Doviak and Zrnic 1993). The beam illumination function acts as a three-dimensional filter on the radial velocity field. It can be approximated by the product of a rectangular filter in the beam direction, and two Gaussian filters in the directions perpendicular to the latter. The random motion of the scatterers within the pulse volume increases the Doppler spectrum width. A reliable estimate of the first moment can only be obtained by averaging multiple samples. This, combined with the spatial displacement of the beam due to the platform motion, produces a further filtering in space and time.

The reduction in the error of the estimate of the mean Doppler, for large SNR and narrow spectrum widths, can be expressed (Doviak and Zrnic 1993), as:

$$\sigma_{\mathrm{v}}^2 \approx \frac{\lambda \mathrm{PRF} \sigma_d}{8\sqrt{\pi} M_{\mathrm{pp}}} \tag{29}$$

where PRF is the pulse repetition frequency, σ_d is the Doppler spectrum standard deviation and M_{pp} the number of independent pulse-pairs. Processes that contribute to the Doppler spectrum variance are wind shear (σ_s^2), turbulence (σ_t^2), particle fall-speed distribution (σ_f^2), and spectrum broadening due to platform motion (σ_p^2) (Nathanson 1969; Jorgensen et al. 1983; Doviak and Zrnic 1993). These processes can be considered independent of one another, thence the total variance can be expressed as the sum of the individual contributions:

$$\sigma_d^2 = \sigma_s^2 + \sigma_f^2 + \sigma_p^2 + \sigma_t^2 \tag{30}$$

The contribution to the beam broadening due to the aircraft is a function of the aircraft air-speed, the beam orientation (ϵ_1) with respect to the aircraft velocity vector $\vec{v}_{\mathrm{AC}}$, and the radar two-way half-power beamwidth (θ_2) (Jorgensen et al. 1983):

$$\sigma_p^2 = (0.42\, v_{\mathrm{AC}}\, \theta_2 \sin \epsilon_1)^2 \tag{31}$$

For the typical WCR/UWKA $\sim$90 m s^{-1} airspeed and $\sim$0.76° beamwidth angle, σ_p^2 is on the order of $\sim$0.16-0.25 m^{2}s^{-2}.

The variance of the radial velocity solely due to the hydrometeor size distribution ($n_d(D)dD$) within the pulse volume may be written as:

$$\begin{cases} \sigma_f^2 = \dfrac{\int_0^\infty n_d(D) D^6 (v_t(D) - \tilde{v}_t)^2 dD}{\int_0^\infty n_d(D) D^6 dD} \cos^2(\epsilon_2) \\ \tilde{v}_t = \dfrac{\int_0^\infty n_d(D) D^6 v_t(D) dD}{\int_0^\infty n_d(D) D^6 dD} \end{cases} \tag{32}$$

where D is the particle diameter and $v_t(D)$ its terminal velocity; $\tilde{v}_t$ is the reflectivity weighted average terminal velocity of the ensemble and ϵ_2 the angle between the beam and the vertical direction. Eq. (32) assumes that the reflectivity (and $n_d(D)$) is homogeneous within the pulse volume, so that the beam illumination function does not play a role.

Terminal velocities for cloud droplets at standard atmospheric conditions only range from 0.003 to 0.074 m s^{-1} (for a 10-50 µm diameter droplet, Khvorostyanov and Curry (2002); Rogers and Yau (1989)). For comparison, the fall speed of a 100 µm drizzle drop is $\sim$0.4 m s^{-1}. These values scale with altitude according to the square of the density ratio between standard sea-level air density and density at the cloud altitude. For instance, at 500 mbar this translates into a $\sim$30% faster terminal velocity. Cloud droplets can thus by large be considered passive tracers for turbulence in the atmosphere, and σ_f^2 can be negligible being on the order of a few cm^{2}s^{-2}(Kollias et al. 2001).

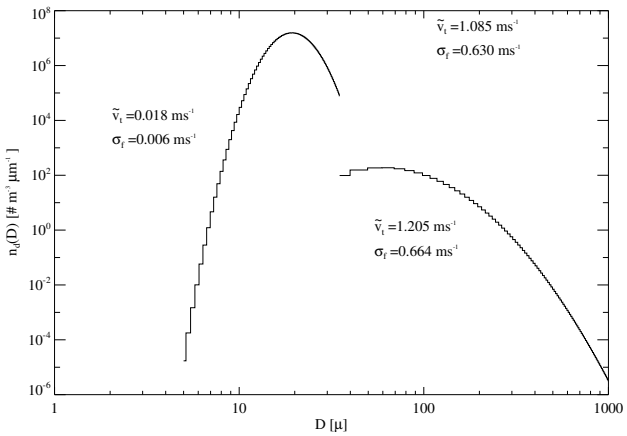

FIG. 9. Assumed log-normal distribution for cloud and drizzle size droplets. The total reflectivity-weighted terminal velocity and Doppler spectrum standard deviation are given at the top of the plot. The contributions from the individual distributions are indicated near the two curves. A vertically pointing beam is assumed.

Figure 9 presents two log-normal spectra describing the size distributions of cloud and drizzle droplets in a typical strato-cumulus cloud. The Doppler spectrum variance due to the terminal velocity of the particles from those distributions is on the order of 0.36 m^{2}s^{-2}. A more convective cumulus cloud might have a narrower cloud droplet distribution, but, at low temperatures, may also contain ice crystals with opposite effects on the Doppler spectrum width. The proposed value for σ_f is then still acceptable except in presence of large graupel or hail. The spectrum variance for small ice crystals to large snowflakes is on the order of 0.04-0.2 m^{2}s^{-2} (Lhermitte 1971). In presence of hail, σ_f, almost entirely due to the largest hydrometeor contribution, may be on the order of 1-4.5 m s^{-1} (Lhermitte 1971). For rain drops $\sigma_f \approx$1 m s^{-1} is generally adopted (Lhermitte 1971; Doviak and Zrnic 1993).

The shear contribution to the Doppler spectrum width, for a quasi-axisymmetric beam shape, can be calculated (Doviak and Zrnic 1993) as:

$$\sigma_s^2 = \frac{\theta_2^2}{16 \ln 2} r^2 (k_\vartheta^2 + k_\varphi^2) + (0.35 r_s k_r)^2 \qquad (33)$$

where k_ϑ, k_φ, k_r are radial velocity shears along the three orthogonal directions (r,ϑ,φ) of the spherical reference frame within the beam pulse volume at range r; θ_2 is the radar two-way half-power beamwidth, and r_s is the range resolution. Adopting a maximum range of 3 km, $\theta_2 = 0.76°$, $r_s \simeq$45 m, and a uniform shear of 0.05 s^{-1}, Eq. (33) yields $\sigma_s \simeq$1.33 m^{2}s^{-2}. For a 0.1 s^{-1} shear σ_s^2 =5.3 m^{2}s^{-2}. For fair weather cumuli, where variations in vertical velocities of about 2 m s^{-1} may occur within the resolution volume, σ_s^2 can reach 1.6 m^{2}s^{-2} (Kollias et al. 2001).

The Doppler spectrum variance due to turbulence, σ_t^2, can be calculated (Eq. (34)) as the integral of the turbulent energy spectrum $\Sigma_t(\tilde{k}) = A_t \epsilon^{2/3} \tilde{k}^{-5/3}$, where: A_t is a universal constant (between 1.53 and 1.68 (Gossard and Strauch 1983, p.262)), ϵ is the eddy dissipation rate, and $\tilde{k} = 2\pi/l$ is the wavenumber related to the length scale l.

$$\sigma_t^2 = \int_{2\pi/l_v}^{2\pi/l_\lambda} \Sigma_t(\tilde{k}) d\tilde{k} = \frac{3A_t}{2} \left(\frac{\epsilon}{2\pi}\right)^{2/3} (l_v^{2/3} - l_\lambda^{2/3}) \qquad (34)$$

Eq. (34) supposes that the length scales l_λ and l_v are contained in the inertial subrange, which in the lower atmosphere includes eddy sizes from a few centimeters to hundreds of meters. It is common practice to accept the Kolmogorov length scale as the lower bound for the inertial subrange. The inner scale of the inertial subrange identifiable by the radar is, however, limited to $l_\lambda = \lambda/2$, i.e., half the radar wavelength. Similarly, for the outer scale probed by the radar, l_v, the pulse volume characteristic size, including the large eddies advected across the pulse volume during the scan dwell time, can be assumed.

For our purposes, an estimate of σ_t^2 can be obtained by using Eq. (34) and assigning typical measured values of ϵ. The highest values of dissipation rate in severe storms are on the order of 1 m^{2}s^{-3} (Doviak and Zrnic 1993). For moderate storms ϵ =0.06 m^{2}s^{-3}, with the largest values usually observed at the interface between updrafts and downdrafts (Frisch and Strauch 1976; Doviak and Zrnic 1993; Kollias et al. 2001). Fair weather cumuli present dissipation rates of about 0.02 m^{2}s^{-3} (Kollias et al. 2001). For the cases presented in Section 6, it is reasonable to estimate the upper bound of ϵ at 0.06 m^{2}s^{-3}. For l_λ =0.0015 m ($> l_k$), l_v =45 m, A_t =1.6, Eq. (34) yields σ_t^2 =1.4 m^{2}s^{-2}. In the literature, the reported maximum values of σ_t^2 for cumuli are about 1.44 m^{2}s^{-2} (Kollias et al. 2001), and 0.1-20.25 m^{2}s^{-2} for light to strong precipitation systems (Lhermitte 1971).

Using Eq. (30) and the estimated values for the various contributions, σ_d^2 is then given by :

$$\sigma_d^2 = (1.33 \div 5.3) + (0.36 \div 20) \cos^2 \epsilon_2 + (0.16 \div 0.25) \sin^2 \epsilon_1 + (1.4 \div 20) \text{m}^2\text{s}^{-2} \qquad (35)$$

where we may identify a lower (upper) bound for a convective cloud in absence (presence) of strong precipitation, function of the orientation of the beam with respect to the vertical and to the AC motion direction. Values are given in Table 5.

5.7 *Uncertainties due to Low SNR*

Equation (29) is valid for high signal-to-noise ratios. A more general expression for the variance of the mean Doppler, under the hypothesis of a large number of independent samples, is (Doviak and Zrnic 1993, Eq.(6.21)):

$$\sigma_{v\,\text{SNR}} = \lambda^2 (32\pi^2 M_{pp} \hat{\rho}^2 t_{pp}^2)^{-1} \left[\left(1 + \text{SNR}^{-1}\right)^2 - \hat{\rho}^2 \right] \qquad (36)$$

variances	nadir		down-fwd		side		side-fwd	
(units: m^2s^{-2})	weak	severe	weak	severe	weak	severe	weak	severe
σ_s^2	1.33	5.3	1.33	5.3	1.33	5.3	1.33	5.3
σ_f^2	0.36	20.25	0.29	16.36	0		0	
σ_p^2	0.25		0.20		0.25		0.16	
σ_t^2	1.4	20	1.4	20	1.4	20	1.4	20
σ_d^2	3.34	46.05	3.22	42.11	2.98	25.80	2.89	25.71
σ_v^2	0.27	1.01	0.27	0.96	0.26	0.75	0.25	0.75

Table 5. Contributions to the Doppler spectrum variance and final error in the mean Doppler (cf. Eq. (29) - (30) for the WCR/UWKA antenna installation. M_{pp} =30 and PRF =20 kHz assumed.

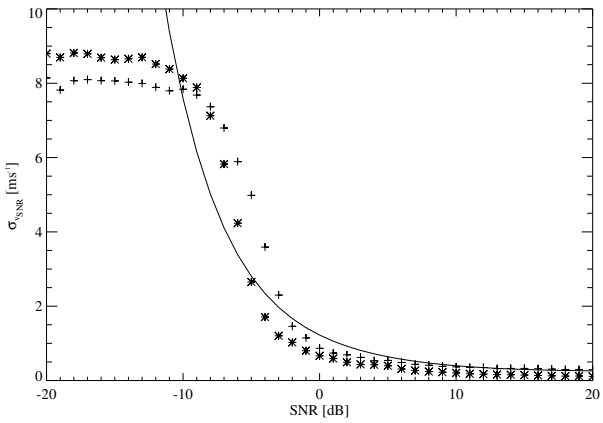

FIG. 10. Theoretical (solid line) and data-derived standard deviations of the mean Doppler as a function of the SNR. For the theoretical one: $M_{\text{pp}} = 30$ and $\sigma_d \approx$1.8 m s^{-1}. Crosses: side-straight beam; stars: side-forward beam. The data belong to an HBDD analysis of a Cu performed on July 20, 2003.

where M_{pp} is the number of independent pulse-pairs, $\hat{\rho} = \hat{\rho}(t_{pp})$ is the signal sample correlation coefficient at lag t_{pp} which is the intra-pulse-pair time interval. Eq. (36) can be utilized to devise a weighting function to limit errors among the points belonging to a given cell, which may be affected by different SNR as mentioned in Section 4.3. In Fig. 10, the theoretical expression in Eq. (36) is plotted together with an empirical one for $\sigma_{\text{v SNR}}$ based on HBDD straight and slanted-pointing beam data. The curves asymptotically tend to $\sigma_d/\sqrt{M_I}$ for high SNR. For low SNR, the empirical curves tend to the standard deviation of a noise uniform distribution $\in [-v_{\text{nyq}}; v_{\text{nyq}})$. The discrepancy with the theoretical trend is due to the Eq. (36) missing the detectability issue of a real system. Furthermore, the data-derived curve is an average for the whole data-set, whereas the theoretical one refers to a single target. The two are, nevertheless, in good agreement and thus they can be used to weight (and cut-off) the data points.

5.8 *Uncertainties due to the Temporal Evolution between Illuminations*

A further source of uncertainty in the dual-Doppler analysis comes from the target advection and the 'intrinsic' evolution (i.e., the field variation observed in a reference moving with the storm) in the time interval between the two beam illuminations. A rigorous treatment of the problem is offered in Chong et al. (1983) and Gal-Chen (1982), together with correction algorithms to limit errors from advection effects and to link the intrinsic temporal variation to the scale of the motion.

For the geometry of the UWKA/WCR installation, the time lag between the two radiations is modest, increasing with the range roughly from 0.9 s at 150 m to 19 s at 3 km from the AC. This time interval is an order of magnitude less than that of a classic ground-based or airborne dual-Doppler realization (cf. Hildebrand and Mueller (1985); Ray and Jorgensen (1988)). The errors are partially reduced in an airborne execution since the aircraft is usually flown so to attain a Lagrangian observation of the target.

The technique presented here advects the grid according to an estimate of the mean wind from flight level records or from another source estimating the storm motion. Significant errors are thus limited only to the presence of unaccounted shear or to the effects caused by the characteristic time evolution of the features of scales captured by the grid resolution. Typical time scales for eddies in cumulus convection, for instance, are on the order of minutes. Smaller scale turbulence cannot be captured with this type of analysis. An error of 5 m s^{-1} in the mean wind estimate can translate at large ranges ($>$2 km) into one grid-spacing error, i.e., the distance traveled by the scatterers in the time interval between scans. Since the grid cannot resolve features at scales less than twice the grid spacing, this error is usually acceptable. A degrading grid resolution with the range can be employed to offset it.

Vertical scatterer velocities are generally (except for severe storms) $<$10 m s^{-1}. Assuming a null grid vertical advection (i.e., an average null air vertical velocity) should not produce errors larger than those in the horizontal if the grid resolution were stretched along the range; if the grid spacing were kept constant, it might again give rise to one grid-spacing error.

The resulting velocity error $\varepsilon_{\text{v},5}$ can be expressed as $\Delta\, k_{\text{v}}$, where Δ is the grid spacing (or the unaccounted displacement of the scatterer volume) and k_{v} the local gradient of the slanted-pointing beam radial velocity, along either the vertical or horizontal direction. For

r =3 km, Δ =45 m, and k_v =0.005 s^{-1}, the error amounts to 0.22 m s^{-1}. Note that at closer ranges the error is even less and it is partially mitigated by the participation in the velocity calculation of several points within each grid cell.

The errors due to temporal field variation should be regarded as a lower cut-off for the resolvable kinematic scales. Furthermore, a coarser resolution may be envisioned for some cases in order to curb errors via data smoothing.

5.9 *Propagation of the Error from the Radial Velocities to the Retrieved Velocity Vector*

The errors in the radial velocities translate into perturbations of the matrix $[B]$ and the known vector $\underline{v}$ in the system (12). In the solution of the velocity inverse decomposition problem these errors propagate into the retrieved velocity vector, with sensitivity depending on the condition number as mentioned in Section 4.4. If $[E]$ is the perturbation matrix representing the errors in $[B]$, and $\underline{\varepsilon}_v$ the array representing the errors in the known vector $\underline{v}$, it can be proven that if $\vec{v}_{LS} + \underline{\varepsilon}_{LS}$ is a solution of the system $([B] + [E])(\vec{v}_{LS} + \underline{\varepsilon}_{LS}) = \underline{v} + \underline{\varepsilon}_v$, then the following bound (Lawson and Hanson 1974) for the error $\underline{\varepsilon}_{LS}$ in the solution of the least-squares problem exists:

$$\frac{\|\underline{\varepsilon}_{LS}\|}{\|\vec{v}_{LS}\|} \leq \frac{\kappa}{1-\kappa\boldsymbol{\alpha}}[(2+\kappa\frac{\|\underline{\mu}\|}{\|[B]\|\|\vec{v}\|})\boldsymbol{\alpha}+\frac{\|\underline{\varepsilon}_v\|}{\|[B]\|\|\vec{v}\|}] \quad (37)$$

where $\kappa = \|[B]\|\|[B^+]\|$ is the generalized matrix condition number, $\boldsymbol{\alpha} = \|[E]\|/\|[B]\|$, and $[E]$ is assumed to satisfy the inequality $\|[E]\|\|[B^+]\| < 1$.

A simplified expression for the upper bound of the final velocity error, as a function of that in the individual radial velocities, is given in what follows.

Denoting $\varepsilon_{v\,i}$ the generic error in the radial velocity v_i, including those due to the wrong assumption of the beam pointing directions $\vec{b}_i$, and $\vec{v}$ and $\vec{v}_a$ the retrieved and actual velocity vector respectively, it can write:

$$\vec{v} \cdot \vec{b}_k = v_k + \varepsilon_{v\,k}, \quad k = 1 \ldots m \quad (38)$$

where m data points participate in the velocity inverse decomposition problem. Noting that $\vec{v}_a \cdot \vec{b}_k = v_k$, Eq. (38) yields:

$$[B]\vec{\varepsilon}_v = \underline{\varepsilon}_v \quad (39)$$

where $[B]$ is the matrix of the beam direction cosines (cf. Section 4.4) and $\vec{\varepsilon}_v$ is the error in the final velocity vector. The same least-squares solution applied to the velocity retrieval can be used to solve Eq. (39), thus the following writes:

$$\|\vec{\varepsilon}_v\| \leq \|[B^+]\|\,\|\underline{\varepsilon}_v\| \quad (40)$$

where $[B^+]$ is defined in Eq. (15).

In Table 6, two estimates for $\frac{\|\vec{\varepsilon}_v\|}{\|\vec{v}_{LS}\|}$ are offered based on Eq. (37) and on the simplified Eq. (40), whose assessed terms are also given in the Table. A generic (20×3) matrix $[B]$, equally subdivided in data coming from 10 straight- and 10 slanted-pointing beam unit vectors, is assumed. The retrieved velocity vector magnitude is estimated in 10 m s^{-1}, and the $[E]$ matrix is based on the standard deviations of the beam direction cosines (cf. Table 3). The residual norm is taken equal to 0.1 m s^{-1}. The norm of the radial velocity array $\underline{v}$ is estimated considering the actual velocity at 45° with respect to the straight-pointing beam. The $\underline{\varepsilon}_v$ generic element is assumed equal to 0.5 m s^{-1}, or 0.75 m s^{-1} for Eq. (40) where the errors of the beam unit vectors are also included in this term.

If $[E] = [0]$, including the effects of the beam unit vectors in the $\underline{\varepsilon}_v$ vector, Eq. (37) yields relative errors less than 20%.

Note that, from Table 6, the error appears larger for VPDD than for HBDD. This is caused by the larger condition status of the matrix $[B]$ for the former, where the beam directions are slightly closer to being collinear (cf. Fig. 1) than the respective ones for HBDD. Nonetheless, for what said in the previous sections, the HBDD analysis is prone to larger errors in the radial velocities (due to the beam direction estimates for example). Moreover, VPDD analyses are usually affected by errors smaller than those assumed in Table 6, yielding final uncertainties in the retrieved velocity smaller than the HBDD counterpart.

The error in the velocity components, and thus on the velocity direction, is derivable from that in the magnitude via vector decomposition. In the assumed case, the components are affected by about 70% of the calculated magnitude error.

6. CASE STUDIES

In the following two sections, results of two dual-Doppler analyses are briefly outlined showing the capabilities of the proposed technique. The cases are from cumulus cloud investigations during the HiCu03 field experiment (`http://www-das.uwyo.edu/wcr/projects/hicu03/hicu03.html`). The kinematic fields are to be considered relative to a frame translating with the mean ambient wind measured at flight level. The straight-pointing beam reflectivity, interpolated onto the grid, has been chosen to display in the background of the figures.

6.1 *VPDD*

Fig. 11 presents results of a VPDD analysis for an emerging tower in a well developed congestus. The cloud base altitude was about 4900-5000 m (standard atmosphere pressure altitude).

In the central portion of the cloud the echoes are weak, with the highest values visible at the top and along the sides. The updraft is carrying very small water droplets while larger hydrometeors form higher up and precipitate along the sides of the cloud. The fine resolution allows to capture the kinematics of small features and entrainment episodes: at the very top of the cloud, for instance, dry ambient air is engulfed by the overturning motion of a 200 m wide turret. Inside the cloud, the larger scale vorticity can be interpreted as a tilted vortex-ring structure (Damiani et al. 2004, 2005) associated with the central updraft: a clockwise circulation is visible centered at 5300 m along the track and at an altitude of 6100 m; a counterclockwise vortex is centered at 4600 m along the

	$\|\|[B]\|\|$	$\|\|[E]\|\|$	$\|\|[B^+]\|\|$	$\|\|\vec{v}\|\|$	$\|\|\underline{v}\|\|$	$\|\|\underline{\varepsilon}_v\|\|$	$\|\|\underline{\mu}\|\|$	$\frac{\|\|\underline{\varepsilon}_{LS}\|\|}{\|\|\underline{v}_{LS}\|\|}$
units	–	–	–	m s^{-1}	m s^{-1}	m s^{-1}	m s^{-1}	[%]
VPDD	4.33	0.04	0.88	10.00	26.77	2.24(3.35)	0.1	27(30)
HBDD	4.24	0.06	0.70	10.00	26.77	2.24(3.35)	0.1	26(24)

Table 6. Estimates of the terms appearing in Eq. (37) (and Eq. (40) in parentheses) for the upper bound of the error in the velocity vector. More in text.

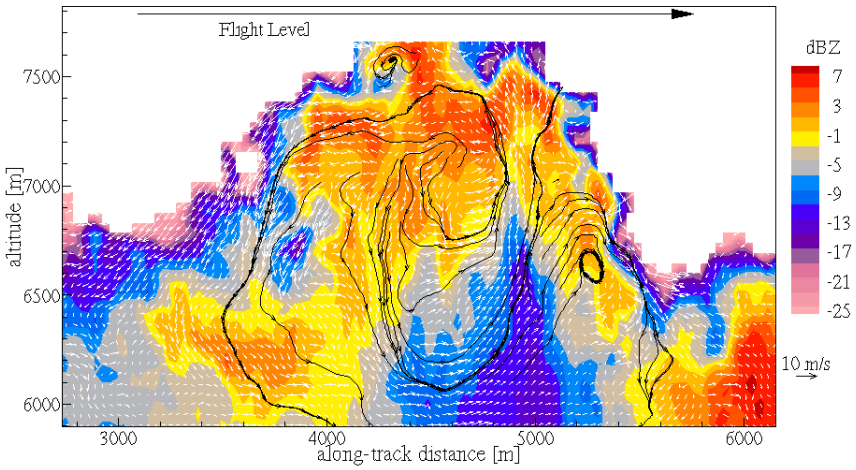

FIG. 11. VPDD analysis for a cumulus cloud investigated on July 31, 2003. Time 191600 UTC. Grid orientation is 75°. Grid resolution 33*46 m^2. Data have been weighted and thresholded based on the SNR and the Inverse Distance Weighting function.

track and 6600 m altitude. The weak echo to the left of the latter structure is likely the consequence of a previous entrainment episode associated with vortex-driven dry air engulfment (see the deep dent in the cloud left boundary).

The mean and standard deviation of the residual-vector norm are ∼0.14 m s^{-1} and ∼0.28 m s^{-1} respectively. The largest values are found along the edges of the cloud, but within most of the cloud domain the residual is less then 0.1 m s^{-1}, about one order of magnitude below the uncertainties in the matrix $[B]$ and vector $\underline{v}$. The highest residual norm corresponds to cells associated with low SNR and with solution system ranks less than 2.

In Fig. 12, the upper bound for the velocity magnitude error (absolute value) is plotted for each grid cell according to Eq. (37) and to the actual values of the norms of the matrices and vectors $[B]$, $[B^+]$, $\vec{v}$, $\underline{v}$, $\underline{\mu}$, and the best estimates for the norm of $\underline{\varepsilon}_v$. The total error in the radial velocity was calculated as the root-square-sum of all the error contributions. Uncertainties on the beam direction cosines were based on the lower values of Table 4. The contribution to the error from the Doppler spectrum width (cf. Section 5.6) was estimated from the autocovariance-process-derived Doppler spectrum standard deviation (Doviak and Zrnic 1993).

Time evolution/advection effects were evaluated according to the discussion in Section 5.8. The beam-point unaccounted displacements were calculated based on the UWKA airspeed and assuming the error in the advection/evolution velocity equal to the locally retrieved velocity, relative to the assumed mean wind. The radial velocity gradients were estimated from the measured slanted-pointing beam Doppler velocities, and, for displacements larger than one grid spacing, they were bounded to a more realistic 0.005 s^{-1}. The beam reciprocal misalignment was evaluated based on the in-flight measured $\sigma(\beta) \simeq 0.53°$, and on a gradient of the radial velocity along the normal to the grid plane of 0.005 s^{-1}.

Further errors (up to 0.5 m s^{-1} for the type of cloud under investigation) could be introduced if the velocity were to be considered as air and not scatterer velocity. Furthermore, an unaccounted ambient vertical shear could produce bias errors in the subtracted mean ambi-

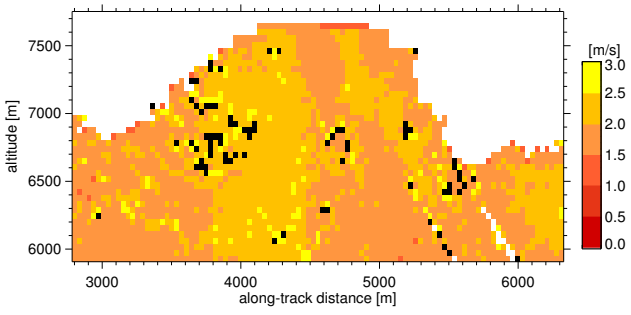

FIG. 12. Upper bound of the error in the retrieved velocity magnitude, according to Eq. (37) and assuming all the errors in the array $\underline{\varepsilon}_v$.

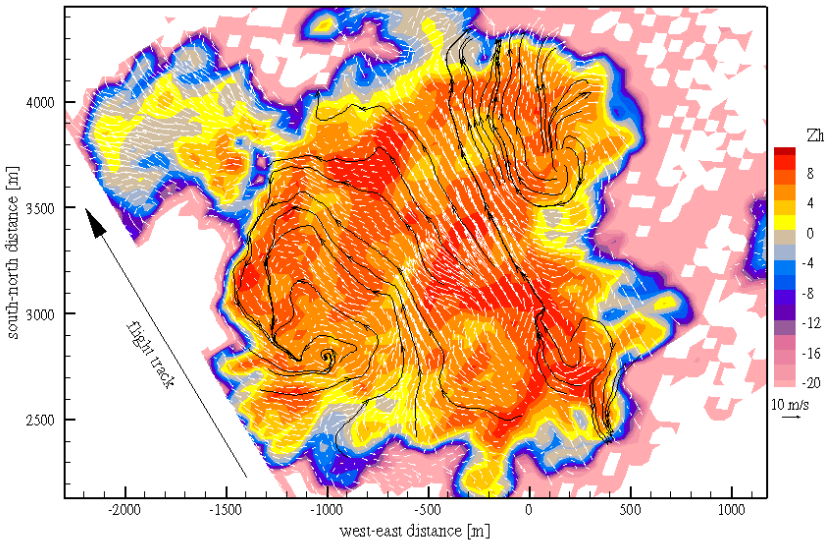

FIG. 14. HBDD analysis for a cumulus congestus investigated on July 12, 2003. Time 193530 UTC. Heading is 330°. Grid resolution 35*46 m^2. Data have been weighted and thresholded based on the SNR and the Exponential Weighting function (c_{exw} =0.1, ROI =35 m).

ent wind, amounting to about 3 m s^{-1} at ranges beyond say 1 km. These effects are difficult to evaluate without a near-by sounding and an accurate knowledge of the microphysical composition of the cloud. Sidelobe effects are deemed negligible as well as the errors deriving from the mis-accounting of the wind cross-plane component (since the flight attitude was characterized by $\sigma_\psi \simeq \sigma_\theta \simeq \sigma_\phi \simeq 1.5°$).

The error upper bounds for the components of the velocity vector (and thus for its direction) can be calculated by decomposing the error in the magnitude along the ξ and η directions, starting from the locally retrieved velocity one. They are on the order of the magnitude error.

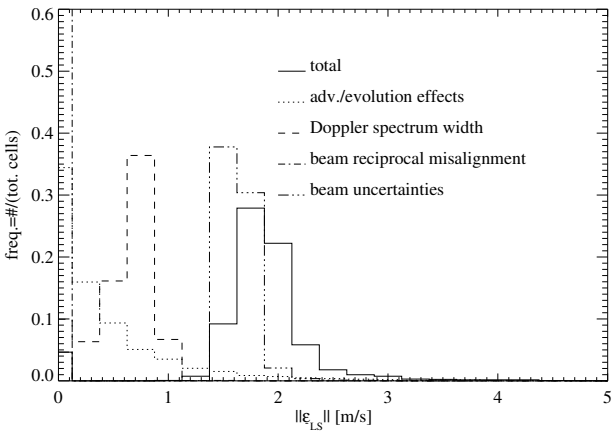

FIG. 13. Distribution of the total and individual contributions to the error upper bound of Fig. 12 for the grid domain shown in this section.

In Fig. 13, the frequency distribution of the total and partial error bounds is presented. The mean and standard deviation of the total error bound are 1.78 m s^{-1} and 1.73 m s^{-1} respectively, and the 90% percentile is 2.36 m s^{-1}. The largest contributions come from: the uncertainty in the beam unit vectors, the spread of the Doppler power spectrum and the unaccounted advection/evolution effects.

6.2 *HBDD*

On July 12, 2003 a series of congesti with high bases (approximate altitude 5300 m) were investigated.

In the case shown in Fig. 14, the HBDD retrieved velocity field is interested by a pair of large-scale (∼500 m) counter-rotating vortices. Horizontal plane entrainment is visible at the edges of the cloud. The reflectivity contours show that weak echo branches extend from the edges towards the interior of the cloud wrapping around the major vortices. The generation of vertical vorticity (in absence of ambient shear in the horizontal plane) is not clear. Potential mechanisms include tilting of horizontal vorticity and slanted ascent of vortex rings (of the type depicted in Fig. 11). Maximum values of the calculated vertical vorticity (not shown) are in excess of 0.05 s^{-1}.

The mean residual vector norm for this analysis is 0.12 m s^{-1} with a standard deviation of 0.15 m s^{-1}. The upper bound of the error in the retrieved velocity, according to Eq. (37), is shown in Fig. 15. Analogous assumptions to those for the VPDD case in Section 6.1 were

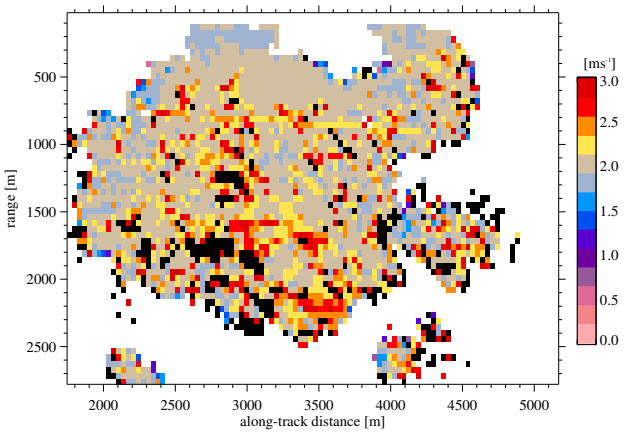

FIG. 15. Upper bound of the error in the retrieved velocity magnitude, according to Eq. (37) and assuming all the errors in the array $\underline{\varepsilon}_v$.

used. The beam reciprocal misalignment was evaluated from the flight-measured $\sigma(\alpha) \simeq 0.94^\circ$, and a gradient of the radial velocity, along the normal to the grid plane, of 0.005 s^{-1}. The mean value for the error upper bound is 1.85 m s^{-1} with standard deviation equal to 1.33 m s^{-1}, and the 90% percentile is 2.89 m s^{-1}.

From the frequency distribution of the error (not shown), it can be inferred that the largest contributions still come from the mis-representation of the AC motion along the beam directions, Doppler power spectrum width, and the mis-accounted advection/evolution effects. Compared to the VPDD case, the errors are larger mainly due to the larger uncertainties in the beam directions.

In Fig. 16, the same case is analyzed with a curtain-leg grid. A larger swath was adopted to include slanted-pointing beam points along the cloud edges farther from the AC, which would have been cut-off otherwise. The median value for the point-swath is $\sim$25 m; at far ranges, however, beam points reach distances of $\sim$150 m from the grid plane. Since the swath is measured perpendicular to the local plane of the cells, its value is now larger than in the case of straight-leg ($<$90 m), where the horizontal plane grid smooths out this effect. Such a large swath is caused by the sharp roll-variations of the AC at the points indicated by the arrows in the Figure. The side-forward-pointing beam is projected higher than the plane swept by the side-pointing one in correspondence of the region in the circle marked in Fig. 16. As a consequence, the kinematic feature within the circle can be interpreted as real only if a continuity of the same amount as the swath in the normal-to-grid direction is accepted. If a 0.005 s^{-1} shear perpendicular to the grid existed, the uncertainty error in that region would increase by about 0.75 m s^{-1}.

This example clarifies how the curtain-grid methodology can be used to identify suspicious regions and to evaluate further errors in the velocities and in the interpretation of kinematic structures.

7. CONCLUSIONS

We have described a new approach for the realization of an airborne dual-Doppler analysis via a re-gridding procedure of fixed-beam data and a velocity inverse decomposition algorithm. The resolution of the grid is in the order of 30-50 m.

The problem reduces to solve a linear system of equations, mostly overdetermined but rank deficient, for every grid cell, via a weighted least-squares method. To retrieve the 2-D velocity vector in the plane of scan, a guess of the cross-plane component is also necessary. Contamination from horizontal wind into VPDD-retrieved vertical motion can otherwise be important in cases where the aircraft attitude significantly deviates from straight and level flight. In case of HBDD scans these errors are contained as the vertical air speed is usually less than, or at least not as uniform as, the horizontal wind.

The overall accuracy of the retrieved velocity fields is on the order of 1-2 m s^{-1}, in absence of further smoothing or of iterative integration of the mass continuity equation. The technique, in fact, produces smooth velocity fields even though each cell data point is uniquely and independently calculated. Forcing the 2-D continuity, as for instance in Weiss and Bluestein (2002), could constitute a further error source rather than be beneficial in certain cases. The three-dimensionality of cumulus cloud flow is, for instance, a strong impediment to the application of the mass budget in a 2-D plane. In transects across quasi-2-D density currents, however, the continuity equation could be used to smooth the field even further.

The uncertainty in the final velocity vector depends on a number of causes. They were described and the errors quantified with reference to particular weather target characteristics. Error sources include uncertainties associated with: the specific radar and its processing system, SNR effects on the Doppler spectrum width, the knowledge of the platform motion, the antenna beam pointing angles and potential reciprocal misalignment due to aircraft attitude variations, the external wind information, the temporal variation of the target between beam scans, interpolation effects, scatterer terminal velocity, and the weather target properties (shear, scatterers distribution etc...).

The technique was successfully applied to the UWKA-WCR installation. Two case studies have been offered for cumulus clouds. The error upper bound was quantified, with the largest contribution coming from the beam direction ambiguity, the Doppler power spectrum broadening, and the temporal evolution effects. To reduce the first, a specific set of flight maneuvers could be devised in order to reduce the standard deviation of the beam pointing angles. The Doppler spectrum could be made narrower by increasing the number of independent sample averages by trading-off the along-track resolution. The third error source may not be avoidable in some cases; the grid resolution could be degraded in order to partially overcome time evolution effects via data smoothing, although this will reduce the small-scale capturing capabilities of the technique and data-filtering may become necessary to

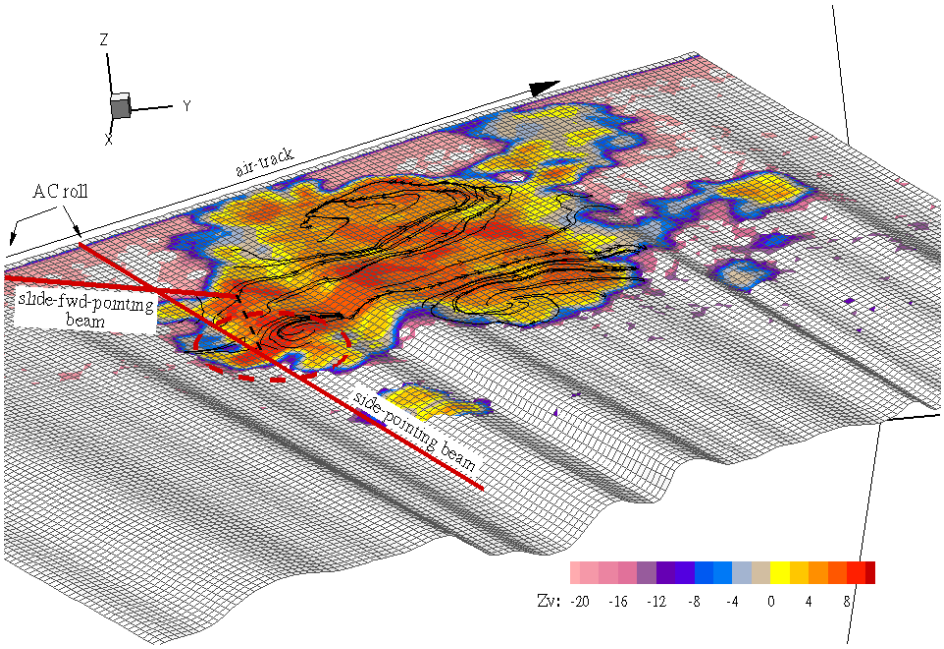

FIG. 16. As in Fig. 14 but with the curtain-leg gridding. Aspect ratio is 1:1:1 along x,y,z.

avoid potential aliasing.

Acknowledgments. The authors would like to thank the colleagues in the Department of Atmospheric Science at the University of Wyoming and the UWKA facility team involved in the HiCu03 experiment. This study was supported by NSF Grant ATM-0094956.

8. REFERENCES

Atkins, N. T., R. M. Wakimoto, and T. Weckwerth, 1995: Observations of the sea-breeze front during CaPE. Part II: Dual-Doppler and aircraft analysis. *Mon. Wea. Rev.*, **123**, 944–969.

Atlas, D., R. C. Srivastava, and R. S. Sekhon, 1973: Doppler radar characteristics of precipitation at vertical incidence. *Rev. Geophys. Space Phys.*, **11**, 1–35.

Brown, E. N., 1993: Measurement uncertainties of the NCAR air motion systems. Technical Report NCAR/TN-386-STR, Research Aviation Facility, Atmospheric Technology Division, National Center for Atmospheric Research, Boulder, CO., nCAR technical note.

Carbone, R. E., M. J. Carpenter, and C. D. Burghart, 1985: Doppler radar sampling limitations in convective storms. *J. Atmos. Oceanic Technol.*, **2**, 357–361.

Chong, M., J. Testud, and F. Roux, 1983: Three-dimensional wind field analysis from dual-Doppler radar data. Part II: minimizing the error due to temporal variation. *J. Climate Appl. Meteor.*, **22**, 1216–1226.

Cressman, G. P., 1959: An operational objective analysis system. *Mon. Wea. Rev.*, **87**, 367–374.

Damiani, R., S. Haimov, and G. Vali: 2004, Velocity fields in cumulus derived from airborne dual-Doppler measurements. *14th International Conference on Clouds and Precipitation, Bologna, IT, June 18-23,2004*, ICCP.

Damiani, R., G. Vali, and S. Haimov, 2005: The structure of thermals in cumulus from airborne dual-Doppler radar observations. *J. Atmos. Sci.*, submitted.

Doviak, R. J. and D. S. Zrnic, 1993: *Doppler radar and weather observations*. Academic Press, 525 B Street, Suite 1900, San Diego, CA 92101-4495, USA, 2nd edition, pp.562.

Frisch, A. S. and R. G. Strauch, 1976: Doppler radar measurements of turbulent kinetic energy dissipation rates in a northeastern Colorado convective storm. *J. Appl. Meteor.*, **15**, 1012–1017.

Gal-Chen, T., 1982: Errors in fixed and moving frame of references: applications for conventional and Doppler radar analysis. *J. Atmos. Sci.*, **39**, 2279–2300.

Gao, J., M. Xue, K. Brewster, and K. K. Droegemeier, 2004: A three-dimensional variational data analysis method with recursive filter for Doppler radars. *J. Atmos. Oceanic Technol.*, **21**, 457–469.

Geerts, B., R. Damiani, and S. Haimov, 2004: Fine-scale vertical structure of a cold front as revealed by an airborne radar. *Mon. Wea. Rev.*, accepted.

Given, T. and P. S. Ray, 1994: Response to a two-dimensional dual-Doppler radar wind synthesis. *J. Atmos. Oceanic Technol.*, **11**, 239–255.

Golub, G. H. and C. F. Van Loan, 1989: *Matrix Computations*. The John Hopkins University Press, 701 W. 40th St., Baltimore, MD 21211, USA, 2nd edition.

Gossard, E. E. and R. G. Strauch, 1983: *Radar observations of clear air and clouds*. Elsevier, 280 pp.

Guyot, A. and J. Testud, 1999: The dual-beam technique applied to airborne cloud radar. *J. Atmos. Sci.*, **16**, 924–938.

Heymsfield, G. M., 1979: Doppler radar study of a warm frontal region. *J. Atmos. Sci.*, **36**, 2093–2107.

Heymsfield, G. M., S. W. Bidwell, I. J. Caylor, S. Ameen, S. Nicholson, B. W., M. L., D. Vandemark, P. E. Racette, and L. R. Dod, 1996: The EDOP radar system on the High-Altitude NASA ER-2 aircraft. *J. Atmos. Oceanic Technol.*, **13**, 795–809.

Hildebrand, P. H., W. C. Lee, C. A. Walther, C. Frush, M. Randall, E. Loew, R. Neitzel, R. Parsons, J. Testud, F. Baudin, and A. LeCornec, 1996: The ELDORA/ASTRAIA airborne Doppler weather radar: high-resolution observations from TOGA CORE. *Bull. Amer. Meteor. Soc.*, **77**, 213–232.

Hildebrand, P. H. and C. K. Mueller, 1985: Evaluation of meteorological airborne Doppler radar. part I: dual-Doppler analyses of air motions. *J. Atmos. Oceanic Technol.*, **2**, 362–380.

Jorgensen, D. P., P. H. Hildebrand, and C. L. Frush, 1983: Feasibility test of an airborne pulse-Doppler meteorological radar. *J. Appl. Meteor.*, **22**, 744–757.

Jorgensen, D. P., T. Matejka, and J. D. DuGranrut, 1996: Multi-beam techniques for deriving wind fields from airborne Doppler radars. *Meteor. Atmos. Phys.*, **59**, 83–104.

Khvorostyanov, V. I. and J. A. Curry, 2002: Terminal velocities of

droplets and crystals: power laws with continuous parameters over the size spectrum. *J. Atmos. Sci.*, **59**, 1872–1884.

Knupp, K. R. and W. R. Cotton, 1982: An intense, quasi-steady thunderstorm over mountainous terrain. Part II: Doppler radar observations of the storm morphological structure. *J. Atmos. Sci.*, **39**, 343–358.

Kollias, P., B. A. Albrecht, R. Lhermitte, and S. A., 2001: Radar observations of updrafts, downdrafts, and turbulence in fair-weather cumuli. *J. Atmos. Sci.*, **58**, 1750–1766.

Kropfli, R. and P. H. Hildebrand, 1980: Three dimensional wind measurements in the optically clear planetary boundary layer with dual-Doppler radar. *Radio Sci.*, **15**, 283–296.

Kropfli, R. A. and L. J. Miller, 1976: Kinematic structure and flux quantities in a convective storm from dual-Doppler radar observations. *J. Atmos. Sci.*, **33**, 520–529.

Lawson, C. L. and R. J. Hanson, 1974: *Solving least squares problems*. Prentice-Hall series in automatic computation, Prentice-Hall, Inc., Englewood Cliffs, N. J., U.S.A.

Lhermitte, R. M., 1971: Probing of atmosphere motion by airborne pulse-Doppler radar techniques. *J. Appl. Meteor.*, **10**, 234–246.

— 1975: Dual-Doppler radar observations and study of sea-breeze convective storm development. *J. Appl. Meteor.*, **14**, 1346–1361.

— 1987: Small cumuli observed with a 3 mm wavelength doppler radar. *Geophys. Res. Lett.*, **14**, 707–710.

— 1988: Cloud and precipitation remote sensing at 94 GHz. *IEEE Trans. Geosci. Remote Sensing*, **26**, 207–216.

Lopez, O. R., A. L. Pazmany, D. Leon, and S. Haimov, 2000: Estimation of cloud attenuation from dual-beam airborne radar measurements. *IEEE*.

Mohr, C. G., L. J. Miller, R. L. Vaughan, and H. W. Frank, 1986: The merger of mesoscale datasets into a common cartesian format for efficient and systematic analyses. *J. Atmos. Oceanic Technol.*, **3**, 143–161.

Nathanson, F. E., 1969: *Radar design principles*. McGraw-Hill, 626 pp.

Pazmany, A., R. E. McIntosh, G. Vali, and R. D. Kelly, 1994: An airborne 95 GHz dual-polarized radar for cloud studies. *IEEE Trans. Geosci. Remote Sensing*, **32**, 731–739.

Ray, P. S., R. J. Doviak, G. B. Walker, D. Sirmans, C. J., and B. Bumgarner, 1975: Dual-Doppler observations of a tornadic storm. *J. Appl. Meteor.*, **14**, 1521–1530.

Ray, P. S. and D. P. Jorgensen, 1988: Uncertainties associated with combining airborne and ground-based Doppler radar data. *J. Atmos. Oceanic Technol.*, **5**, 177–196.

Ray, P. S., D. P. Jorgensen, and S.-L. Wang, 1985: Airborne Doppler observations of a convective storm. *J. Climate Appl. Meteor.*, **24**, 688–698.

Ray, P. S. and K. L. Sangren, 1983: Multiple-Doppler radar network design. *J. Climate Appl. Meteor.*, **22**, 1444–1454.

Ray, P. S., C. L. Ziegler, W. Bumgarner, and J. R. Serafin, 1980: Single- and multiple-Doppler radar observations of tornadic storms. *Mon. Wea. Rev.*, **108**, 1607–1625.

Rogers, R. R. and M. Yau, 1989: *A short course in cloud physics*, volume 113 of *International Series in Natural Philosophy*. Butterworth Heinemann, 3rd edition, pp.290.

Srivastava, R. C. and D. Atlas, 1974: Effect of a finite radar pulse volume on turbulence measurements. *J. Appl. Meteor.*, **13**, 472–480.

Sun, J. and N. A. Crook, 1998: Dynamical and microphysical retrieval from Doppler radar observations using a cloud model and its adjoint. Part II: Retrieval experiments of an observed Florida convective storm. *J. Atmos. Sci.*, **55**, 835–852.

Vali, G. and S. Haimov, 2001: Observed extinction by clouds at 95 GHz. *IEEE Trans. Geosci. Remote Sensing*, **39**, 190–193.

Weiss, C. C. and H. B. Bluestein, 2002: Airborne pseudo-dual Doppler analysis of a dryline-outflow boundary intersection. *Mon. Wea. Rev.*, **130**, 1207–1226.